

Data-driven beamforming technique to attenuate ballistocardiogram artefacts in electroencephalography-functional magnetic resonance imaging without detecting cardiac pulses in electrocardiography recordings

Article

Published Version

Creative Commons: Attribution-Noncommercial-No Derivative Works 4.0

Open Access

Uji, M., Cross, N., Pomares, F. B., Perrault, A. A., Jegou, A., Nguyen, A., Aydin, U. ORCID: <https://orcid.org/0000-0002-6327-7811>, Lina, J.-M., Thanh Dang-Vu, T. and Grova, C. (2021) Data-driven beamforming technique to attenuate ballistocardiogram artefacts in electroencephalography-functional magnetic resonance imaging without detecting cardiac pulses in electrocardiography recordings. *Human Brain Mapping*, 42 (12). pp. 3993-4021. ISSN 1065-9471 doi: 10.1002/hbm.25535 Available at <https://centaur.reading.ac.uk/111220/>

It is advisable to refer to the publisher's version if you intend to cite from the work. See [Guidance on citing](#).

To link to this article DOI: <http://dx.doi.org/10.1002/hbm.25535>

Publisher: Wiley

All outputs in CentAUR are protected by Intellectual Property Rights law, including copyright law. Copyright and IPR is retained by the creators or other copyright holders. Terms and conditions for use of this material are defined in the [End User Agreement](#).

www.reading.ac.uk/centaur










CentAUR

Central Archive at the University of Reading

Reading's research outputs online

RESEARCH ARTICLE

Data-driven beamforming technique to attenuate ballistocardiogram artefacts in electroencephalography–functional magnetic resonance imaging without detecting cardiac pulses in electrocardiography recordings

Makoto Uji¹  | Nathan Cross^{2,3}  | Florence B. Pomares^{2,3}  |
Aurore A. Perrault^{2,3}  | Aude Jegou^{1,4}  | Alex Nguyen^{2,3}  | Umit Aydin^{1,5}  |
Jean-Marc Lina^{6,7} | Thien Thanh Dang-Vu^{2,3}  | Christophe Grova^{1,7,8} 

¹Multimodal Functional Imaging Lab, Department of Physics and PERFORM Centre, Concordia University, Montréal, Québec, Canada

²PERFORM Centre, Center for Studies in Behavioral Neurobiology, Department of Health, Kinesiology and Applied Physiology, Concordia University, Montréal, Québec, Canada

³Institut Universitaire de Gériatrie de Montréal and CRIUGM, CIUSSS du Centre-Sud-de-l'Île-de-Montréal, Montréal, Québec, Canada

⁴Aix-Marseille University, Inserm, INS, Institut de Neurosciences des Systèmes, Marseille, France

⁵Social, Genetic, and Developmental Psychiatry Centre, Institute of Psychiatry, Psychology, and Neuroscience, King's College London, London, UK

⁶Département de Génie Électrique, École de Technologie Supérieure, Montréal, Québec, Canada

⁷Centre de Recherches Mathématiques, Montréal, Québec, Canada

⁸Multimodal Functional Imaging Lab, Biomedical Engineering Department, Neurology and Neurosurgery Department, McGill University, Montréal, Québec, Canada

Correspondence

Makoto Uji and Christophe Grova, Multimodal Functional Imaging Lab, Department of Physics and PERFORM Centre, Concordia University, 7141 Sherbrooke St. West, SP 165.30, Montreal H4B 1R6, Québec, Canada. Email: makoto.uji@concordia.ca (M. U.) and christophe.grova@concordia.ca (C. G.)

Abstract

Simultaneous recording of electroencephalography (EEG) and functional magnetic resonance imaging (fMRI) is a very promising non-invasive neuroimaging technique. However, EEG data obtained from the simultaneous EEG–fMRI are strongly influenced by MRI-related artefacts, namely gradient artefacts (GA) and ballistocardiogram (BCG) artefacts. When compared to the GA correction, the BCG correction is more challenging to remove due to its inherent variabilities and dynamic changes over time. The standard BCG correction (i.e., average artefact subtraction [AAS]), require detecting cardiac pulses from simultaneous electrocardiography (ECG) recording. However, ECG signals are also distorted and will become problematic for detecting reliable cardiac peaks. In this study, we focused on a beamforming spatial filtering technique to attenuate all unwanted source activities outside of the brain. Specifically, we applied the beamforming technique to attenuate the BCG artefact in EEG–fMRI, and also to recover meaningful task-based neural signals during an attentional network task (ANT) which required participants to identify visual cues and respond accurately. We analysed EEG–fMRI data in 20 healthy participants during the ANT, and compared four different BCG corrections (non-BCG corrected, AAS BCG corrected, beamforming + AAS BCG corrected, beamforming BCG corrected). We demonstrated that the beamforming approach did not only significantly reduce the BCG artefacts, but also significantly recovered the expected task-based brain activity when compared to the standard AAS correction. This data-driven beamforming technique appears promising especially for longer data acquisition of sleep and resting EEG–fMRI. Our findings extend previous work regarding the recovery of meaningful EEG signals by an optimized suppression of MRI-related artefacts.

This is an open access article under the terms of the Creative Commons Attribution-NonCommercial-NoDerivs License, which permits use and distribution in any medium, provided the original work is properly cited, the use is non-commercial and no modifications or adaptations are made.

© 2021 The Authors. *Human Brain Mapping* published by Wiley Periodicals LLC.

Funding information

Canadian Institutes of Health Research, Grant/Award Numbers: MOP 142191, MOP-133619, PJT 153115, PJT 156125, PJT 166167, PJT-159948; Natural Sciences and Engineering Research Council of Canada, Grant/Award Numbers: RGPIN-2018-06707, RGPIN-2019-06990

KEYWORDS

ballistocardiogram (BCG) artefacts, beamforming technique, EEG–fMRI, motor beta ERD, time–frequency analysis, visual alpha event-related desynchronization (ERD)

1 | INTRODUCTION

Electroencephalography (EEG) and functional magnetic resonance imaging (fMRI) are two non-invasive neuroimaging techniques that are often used to investigate human brain function, so that their multimodal integration has been actively considered (Jorge, van der Zwaag, & Figueiredo, 2014; Laufs, 2012; Moeller, Siniatchkin, & Gotman, 2020; Murta, Leite, Carmichael, Figueiredo, & Lemieux, 2015). fMRI measures hemodynamic blood oxygen level-dependent (BOLD) responses driven by increased metabolic demands during neuronal activation, which results in indirect measurements of brain activity (Logothetis, Pauls, Augath, Trinath, & Oeltermann, 2001), whereas EEG measures the electrical potentials generated by the cooperative action of neurons providing a more direct measure of neuronal activity (Buzsáki, Anastassiou, & Koch, 2012). Furthermore, fMRI has a high spatial resolution (in order of millimetre) with a poor temporal resolution (in order of seconds) due to slow hemodynamic responses, while EEG generally has a high temporal resolution (in order of milliseconds) with a poor spatial resolution. Simultaneous recording of EEG and fMRI is a very promising non-invasive technique, provides a wide range of complementary information, and can be advantageous for improving our understanding of human brain function.

Studies have demonstrated that simultaneous EEG–fMRI can provide greater specificity and sensitivity when compared to a single neuroimaging modality (EEG or fMRI alone) regarding the spatial arrangement (Goldman et al., 2009; Novitskiy et al., 2011) and the temporal sequence (Eichele et al., 2005; Mayhew, Li, & Kourtzi, 2012) of brain response. For instance, simultaneous EEG–fMRI has been successfully used to investigate epileptic networks in patients with drug-resistant focal epilepsy undergoing pre-surgical evaluation (Gotman, Kobayashi, Bagshaw, Bénar, & Dubeau, 2006; Gotman & Pittau, 2011; Grova et al., 2008; Heers et al., 2014; Ives, Warach, Schmitt, Edelman, & Schomer, 1993; Lemieux et al., 2001; LeVan & Gotman, 2009; Murta, Leal, Garrido, & Figueiredo, 2012), and sleep (Cross et al., 2021; Dang-Vu et al., 2011, 2008; Fultz et al., 2019; Hale et al., 2016) enabling spatial localization of the hemodynamic responses elicited by temporally dynamic specific EEG features/events. Recently, the application of EEG–fMRI has been extended to investigate the spatiotemporal dynamics of neural activity (for a review, see Huster, Debener, Eichele, & Herrmann, 2012), and also to study the underlying neurophysiological origins of the measured responses by comparing neural and hemodynamic signals (Mullinger, Mayhew, Bagshaw, Bowtell, & Francis, 2013). The primary advantage of simultaneous EEG–fMRI acquisition over separate recordings is that it enables the investigation of unpredictable or spontaneous brain

activity, and the study of the trial-by-trial covariation in brain processing as measured by the two techniques (Bagshaw et al., 2004; Becker, Reinacher, Freyer, Villringer, & Ritter, 2011; Debener, Ullsperger, Siegel, & Engel, 2006; Eichele et al., 2008; Goldman, Stern, Engel Jerome, & Cohen, 2002; Horovitz et al., 2008; Mayhew, Ostwald, Porcaro, & Bagshaw, 2013; Mobascher et al., 2009; Mullinger, Mayhew, Bagshaw, Bowtell, & Francis, 2014; Olbrich et al., 2009; Scheibe, Ullsperger, Sommer, & Heekeren, 2010; Uji, Wilson, Francis, Mullinger, & Mayhew, 2018). EEG–fMRI analysis has demonstrated specific BOLD correlates of distinct neurophysiological components including the auditory oddball (Bénar et al., 2007; Eichele et al., 2005) and the error-related negativity (Debener et al., 2005), as well as specific neural activity in specific frequency bands (Goldman et al., 2002; Laufs et al., 2003; Tyvaert, LeVan, Grova, Dubeau, & Gotman, 2008).

However, EEG data obtained from the simultaneous EEG–fMRI recording are strongly influenced by MRI-related artefacts (Allen, Josephs, & Turner, 2000; Allen, Polizzi, Krakow, Fish, & Lemieux, 1998; Niazy, Beckmann, Lannetti, Brady, & Smith, 2005), which are gradient artefacts (GA) and ballistocardiogram (BCG) artefacts. The GA is induced by temporally varying magnetic field gradients used for MR imaging causing large voltage fluctuations in the EEG traces through Faraday's law of induction, 10–100 times larger when compared to EEG signals induced by brain signal (Allen et al., 2000), therefore completely obscuring the measured EEG signal. Since it is generated by the fMRI sequence itself, such artefact is highly reproducible and removal of the GA can be accurately achieved by subtracting averaged GA waveforms measured at each EEG electrode across fMRI volume acquisitions from each corresponding electrode using the average artefact subtraction (AAS) approach.

Compared to the GA, BCG artefacts are definitely more challenging to cope with due to their inherent variabilities and dynamic changes over time (Laufs, Daunizeau, Carmichael, & Kleinschmidt, 2008). The BCG artefact is produced by cardiac pulse driven head motion in the strong magnetic field of the MRI scanner (Debener, Mullinger, Niazy, & Bowtell, 2008; Mullinger & Bowtell, 2011). Therefore, this artefact will be present even when no fMRI acquisitions are performed. Typically, the BCG artefacts obscure the EEG signals below 20 Hz (Bonmassar et al., 2002; Xia, Ruan, & Cohen, 2014, 2013), and this remains problematic especially when the frequency of interest of EEG signals is below 20 Hz, such as alpha (8–13 Hz) and beta (13–30 Hz) band EEG activity, or sleep spindle (11–16 Hz) and slow-wave oscillations (<1 Hz) during sleep. In order to overcome this complexity, both software (independent component analysis [ICA]: Debener et al., 2007; optimal basis set [OBS]: Niazy et al., 2005) and hardware (reference layer artefact subtraction: Chowdhury, Mullinger, Glover, & Bowtell, 2014;

Carbon-wire loop: Masterton, Abbott, Fleming, & Jackson, 2007; Optical Motion tracking system: LeVan et al., 2013) based solutions have been suggested for the BCG artefact correction. Although these different methods have successfully corrected the BCG artefacts, the most commonly used approach is still AAS approach (see a review Abreu, Leal, & Figueiredo, 2018). However, this AAS approach requires high precisions of cardiac pulse (R-peak) event detections in the MRI scanner which are used for subtracting averaged BCG artefact templates. R-peak events are normally detected from simultaneous electrocardiography (ECG) recording, although facial and temporal electrodes of high-density EEG can also be used for the detection (Iannotti, Pittau, Michel, Vulliemoz, & Grouiller, 2015). The ECG signal in the MRI scanner is also often distorted, which makes automatic detection of R-peaks problematic (Chia, Fischer, Wickline, & Lorenz, 2000; Mullinger, Morgan, & Bowtell, 2008), and requires manual correction which is significantly time-consuming. Detecting R-peak events from the ECG is thus difficult, so that this procedure may sometimes become unreliable, although vectorcardiogram (VCG) instead of the ECG recording is more suited and recommended to use for the R-peak detections when available (Mullinger & Bowtell, 2011).

Adapted from the context of EEG and also magnetoencephalography (MEG) source imaging, beamforming technique (Robinson & Vrba, 1999; Sekihara, Nagarajan, Poeppel, Marantz, & Miyashita, 2001; van Drongelen, Yuchtman, Van Veen, & van Huffelen, 1996; van Veen & Buckley, 1988; van Veen, van Drongelen, Yuchtman, & Suzuki, 1997) is a well-known adaptive spatial-filtering approach that also appears as a promising denoising technique, and only recently considered in the context of EEG-fMRI studies (Brookes et al., 2009; Brookes, Mullinger, Stevenson, Morris, & Bowtell, 2008; Mullinger & Bowtell, 2011). The beamforming technique is highly efficient when attenuating artefactual signals which have different spatial origins from the underlying signal of interest, such as eye movements (Cheyne, Bakhtazad, & Gaetz, 2006) and orthodontic metal braces (Cheyne, Bostan, Gaetz, & Pang, 2007) in MEG, and MRI-related artefacts of EEG signal in EEG-fMRI (Brookes, Mullinger, et al., 2008), although the beamforming technique has been initially introduced as a source imaging technique in MEG and EEG studies (Robinson & Vrba, 1999; Sekihara et al., 2001; van Drongelen et al., 1996; van Veen et al., 1997; van Veen & Buckley, 1988). Specifically, the beamforming spatial filter rejects sources of signal variance that are not concordant in predetermined source locations in the brain based on the forward model. Consequently, it attenuates all unwanted source activities outside of the predetermined source location of interest in the data (e.g., eye movements) without having to specify the location or the configuration of these unwanted underlying source signals.

The residual artefacts from the GA and BCG are especially attenuated since their spatial topographies differ from the one corresponding to a dipolar current source located in the brain (Brookes, Mullinger, et al., 2008; Mullinger & Bowtell, 2011). The advantages of the beamforming denoising technique reside in the fact that it is a data-driven approach, which does not require identifying noise and signal components, and does not rely on the detection of ECG R-peaks. The beamforming denoising technique in EEG-fMRI

(Brookes, Mullinger, et al., 2008; Mullinger & Bowtell, 2011) has initially been designed to minimize the residual GA, and normally applied after correcting MRI-related GA and BCG artefact as a post-processing procedure. However, Brookes, Mullinger, et al. (2008) and Brookes, Vrba, et al. (2008) tried the beamforming approach to correct the BCG artefacts without the conventional AAS BCG correction after the GA correction, and demonstrated that the beamforming technique indeed attenuated the BCG artefacts even though this previous work was preliminary and not extensive. In their previous study, this beamforming BCG denoising was examined in the EEG-fMRI data from two healthy adults when they were passively viewing 8.6 Hz flashing checkerboard visual stimuli, and the performance of the beamforming denoising was evaluated by only successfully recovering the second harmonic signals (17.2 Hz) in the source space in the primary visual cortex, when compared to the occipital sensor space signal. With the limited number of participants in the previous study, they did not extend their analysis to examine how much BCG artefact was corrected by the beamforming BCG denoising technique, and did not investigate how much alpha event-related desynchronization (ERD) was observed during the visual stimuli after the proposed beamforming BCG denoising.

In the present study, we proposed to systematically investigate the performance of this data-driven beamforming BCG denoising technique in EEG-fMRI. Therefore, the aim of this work was to investigate whether the BCG artefacts can be attenuated by only using beamforming technique, that is, without taking into account the ECG signal, and also to examine how this technique would preserve expected task-based-induced brain signal in the source space while attenuating the BCG artefacts. To clearly demonstrate the effects of the beamforming BCG artefact correction on EEG task activities, we assessed the effects of beamforming on ERD (reflecting a power decrease) in occipital alpha (8–13 Hz) during the presentation of visual stimuli and motor beta (13–30 Hz) during movement preparation before response onset during an attentional network task (ANT) (Fan et al., 2007; Fan, McCandliss, Fossella, Flombaum, & Posner, 2005). Specifically during the ANT, the visual alpha ERD would be expected during the visual attention before the movement execution cue onset, whereas the motor beta ERD would be expected during the movement preparation/planning before the movement execution (Fan et al., 2007; Marshall, Bergmann, & Jensen, 2015), although the ANT would also induce higher cognitive and attentional processing (alerting, orienting and executive control), which was beyond the scope of this article. In this study, we analysed EEG-fMRI data in 20 healthy participants when they were performing the ANT, and compared the four following BCG correction approaches: non-BCG corrected, AAS BCG corrected, beamforming + AAS BCG corrected, beamforming BCG corrected. We chose to investigate alpha ERD in the visual cortex and beta ERD in the motor cortex since the BCG artefacts typically obscure EEG signal below 20 Hz (Bonmassar et al., 2002; Xia et al., 2014, 2013). Moreover, visual alpha ERD has been well documented during visual stimulations (Brookes et al., 2005; Scheeringa et al., 2011; Wilson, Mullinger, Francis, & Mayhew, 2019), whereas reliable motor beta ERD has been reported

during planning/preparation of the movement (Cheyne & Ferrari, 2013; Darvas et al., 2010; Hall et al., 2011; Muthukumaraswamy, 2010; Pfurtscheller & Lopes da Silva, 1999; Pfurtscheller, Stancák, & Neuper, 1996; Takemi, Masakado, Liu, & Ushiba, 2013; Uji et al., 2018). We hypothesized that the beamforming BCG corrected data would recover visual alpha ERD and motor beta ERD to a similar extent, when compared to the conventional AAS BCG artefact correction and beamforming + AAS BCG corrected data. Furthermore, we also hypothesized that both beamforming approaches would increase the signal-to-noise ratios (SNRs) in the source space when compared to those in the sensor space (Brookes et al., 2009; Hill et al., 2020; Sekihara, Nagarajan, Poeppel, & Marantz, 2004), which should be another advantage of using beamforming technique in EEG-fMRI.

2 | METHODS

The EEG-fMRI data were acquired using a protocol previously published in Cross et al. (2021), and reused for our specific aim to investigate the performance of beamforming denoising technique in simultaneous EEG-fMRI. The original study aimed to examine the effect of sleep deprivation and a subsequent recovery nap on functional connectivity patterns across cognitive tasks of attention, vigilance, and working memory. More details of the study designs and findings can be found in the previous article (Cross et al., 2021).

2.1 | Participants

In this section, 20 young healthy participants (12 females, 8 males, age = 21.3 ± 2.5 years) took part in the study, and were screened for the absence of sleep disorders (insomnia, sleep apnoea syndrome, hypersomnolence, restless legs syndrome, and parasomnias), neurological or psychiatric conditions (e.g., epilepsy, migraine, stroke, chronic pain, major depression, anxiety disorder, psychotic disorder) and current use of psychotropic medications or cannabis. All subjects provided written informed consent prior to the start of the study that was approved by the Central Research Ethics Committee of the Quebec Ministry of Health and Social Services. More details about the participants' characteristics can be found in the previous study (Cross et al., 2021).

2.2 | Experimental procedures

The original experimental procedures can be found in Supplementary Figure S1a. All participants completed three runs of three different cognitive tasks (ANT: Fan, McCandliss, Sommer, Raz, & Posner, 2002; Fan et al., 2005; *Mackworth Clock Task*: Lichstein, Riedel, & Richman, 2000; Loh, Lamond, Dorrian, Roach, & Dawson, 2004; *N-back task*: Kirchner, 1958; Sweet, 2011) during the EEG-fMRI acquisition. Out of these three different tasks, the ANT was chosen as

the most suitable task in order to investigate the performance of beamforming technique in the EEG-fMRI, because it has clear baseline periods and clear event onsets. We predicted that this would induce alpha ERD in the visual cortex and beta ERD in the motor cortex respectively (Fan et al., 2007; Marshall et al., 2015) that would be obscured by the BCG artefacts in the alpha and beta frequency band.

2.3 | ANT paradigm

This task probes different attentional processes, such as alerting, orienting, and executive control (Fan et al., 2002, 2005, 2007) (see Figure 1). The ANT consisted of a series of trials in which the participants were required to identify the direction (left or right) of the middle arrow (target cue) in an array of five arrows within an upper or lower panel of the screen. The middle arrow was either congruent or incongruent to the direction of the other arrows (target cue). Different probing conditions (probe cue) were displayed immediately prior to the appearance of the target cue, including both panels flashing (double cue; alerting), either panel flashing (valid or invalid spatial cues; orienting), or no cue preceding the target cue (no cue). One run of the ANT contained 145 trials in total consisting of 24 double cue trials, 73 valid cue and 24 invalid spatial cue trials, and 24 no cue trials. These trials were also divided into 73 congruent and 72 incongruent trials for the target cue. One run of the task lasted 13 min in duration, with each trial lasting around 1 s with a random jitter (range = 2–12 s, mean = 5 s) between each trial (see more details in Figure 1). In this study, all three runs of the ANT were put together, and all probe cue conditions were treated as the same trials epoching to the target cue onsets (visual epoched trials) and movement onsets (movement epoched trials). The movement epoched trials included both correct and incorrect responses.

The ANT was run on a laptop computer using Inquisit software (Millisecond Software LLC, Seattle, WA), displayed to the participant via a projector screen behind the MRI scanner. The participants responded via button presses made using a response pad attached to the fingers of the left hand. Behavioural outcomes of reaction time (ms) and accuracy (%; correct trials/number of trials) can be found in the supplementary Figure S1b.

2.4 | Simultaneous EEG-fMRI data acquisition

2.4.1 | MRI data acquisition

MRI data were acquired with a 3T GE scanner (General Electric Medical Systems, Milwaukee, WI) using an eight-channel head coil in the PERFORM Centre of Concordia University. Functional MRI were acquired using a gradient-echo echo-planar imaging sequence (repetition time (TR) = 2,500 ms; TE = 26 ms; FA = 90°; 41 transverse slices; 4-mm slice thickness with a 0% inter-slice gap; FOV = 192 × 192 mm; voxel size = 4 × 4 × 4 mm³; and matrix size = 64 × 64). High-resolution T1-weighted anatomical MR images were acquired using a 3D BRAVO

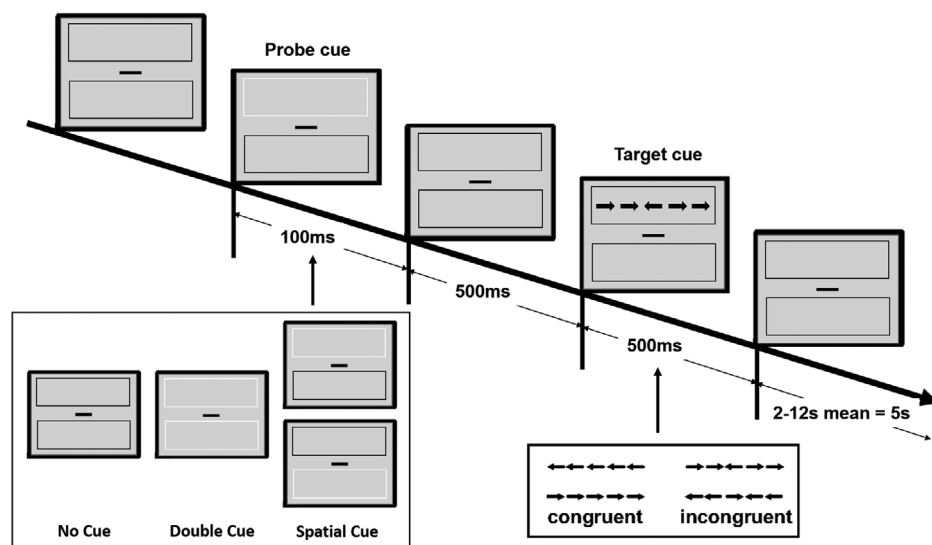


FIGURE 1 Schematic of attentional network task (ANT). In each trial, a fixation cross appears in the centre of the screen all the time. Depending on probe cue conditions, a probe cue (either no cue, double cue, or spatial cue) appears for 100 ms. After a fixed duration (500 ms), a target cue (the centre arrow) among other arrows (congruent or incongruent cue condition) is presented for 500 ms at either an upper or lower panel of the screen, and participants are required to respond via button presses made using a response pad attached to the fingers of the left hand as quickly as possible, but no longer than 1,900 ms after the target cue onset. If participants respond with the correct direction of the middle arrow (left or right) within the time-window, the response is considered as a correct response. A post-target fixation period lasts for a variable duration (inter-trial intervals from the offset of the target cue to the onset of the probe cue during the next trial are randomly jittered between 2,000 and 12,000 ms, mean = 5 s) between each trial. One run of the ANT contained 145 trials in total consisting of 24 double cue trials, 73 valid cue and 24 invalid spatial cue trials, and 24 no cue trials. These trials are also divided into 73 congruent and 72 incongruent trials for the target cue. One run of the ANT lasts around 13 min in duration

sequence (TR = 7,908 ms; TI = 450 ms; TE = 3.06 ms; FA = 12°; 200 slices; voxel size = 1.0 × 1.0 × 1.0 mm, FOV = 256 × 256 mm). During all EEG-fMRI sessions, the helium compression pumps used for cooling down MR components were switched off to reduce MR environment related artefacts infiltrating the EEG signal (Mullinger, Brookes, Stevenson, Morgan, & Bowtell, 2008; Rothluebbers et al., 2015). To minimize movement-related artefacts during the scan, MRI-compatible foam cushions were used to fix the participant's head in the MRI head coil (Mullinger & Bowtell, 2011).

2.4.2 | EEG data acquisition

EEG data were acquired using an MR compatible 256 high-density geodesic sensor EEG array (Electrical Geodesics Inc. (EGI), Magstim-EGI, Eugene, OR). The EEG cap included 256 sponge electrodes referenced to Cz that covered the entire scalp and part of the face. EEG data were recorded using a battery-powered MR-compatible 256-channel amplifier shielded from the MR environment that was placed next to the participant inside the scanning room. The impedance of the electrodes was initially maintained below 20 kΩ and kept to a maximum of 70 kΩ throughout the recording. Data were sampled at 1,000 Hz and transferred outside the scanner room through fibre-optic cables to a computer running the Netstation software (v5, EGI). The recording of EEG was phase-synchronized to the MR scanner clock (Sync Clock box, EGI), and all scanner TRs and participant

responses were recorded in the EEG traces. Especially, the onset of every TR period was marked in the EEG data to facilitate MR GA correction. ECG was also collected via two MR compatible electrodes placed between the fifth and seventh ribs and above the heart close to the sternum, and recorded at 1,000 Hz through a bipolar amplifier (Physiobox, EGI). After the EEG-fMRI data acquisition, EEG electrode locations were digitized using the EGI Geodesic Photogrammetry System (GPS) to facilitate individualized co-registration of electrode positions with each subject's anatomical image (Russell, Jeffrey Eriksen, Poolman, Luu, & Tucker, 2005).

2.5 | Data analysis

In this study, EEG-fMRI data during the ANT in 20 healthy participants were pre-processed, and compared with four different BCG correction approaches (non-BCG corrected, AAS BCG corrected, beamforming + AAS BCG corrected, beamforming BCG corrected) to examine how the beamforming technique would attenuate BCG artefacts and preserve expected brain signal, notably visual alpha ERD and motor beta ERD, induced by the ANT. The four different datasets consisting of non-BCG corrected and AAS BCG corrected sensor level data and beamforming source level datasets from either non-BCG corrected (beamforming BCG corrected) or AAS BCG corrected data (beamforming + AAS BCG corrected) were created in the manner described below.

For both EEG and ECG data, GA were first corrected in BrainVision Analyzer2 (Version 2.2.0, Brain Products GmbH, Gilching, Germany) with the standard AAS method, using sliding window templates formed from the averages of 21 TRs, which were subtracted from each occurrence of the respective artefacts for each electrode (Allen et al., 2000; Wilson et al., 2019). GA corrected data were subsequently band-pass filtered (EEG: 1–100 Hz with notch filter of 60 Hz), and downsampled (500 Hz). Following the GA correction, cardiac R-peaks were automatically detected from the ECG recording in BrainVision Analyzer2, checked visually and corrected manually if necessary, since the ECG signal in the MRI scanner is distorted and has proven to be problematic (Chia et al., 2000; Mullinger, Morgan, & Bowtell, 2008) (Supplementary Figure S2). These R-peak events were used to inform BCG correction of data recording inside the scanner.

From the same GA corrected datasets, two different datasets for each subject were created: non-BCG corrected and AAS BCG corrected data to investigate the effect of beamforming technique on the BCG artefacts or remaining BCG artefacts after AAS BCG correction (Brookes, Mullinger, et al., 2008). The AAS BCG artefact correction was performed using sliding template average-artefact subtraction (11 R-peak events per template) in BrainVision Analyzer2 (Mullinger et al., 2014).

For both non-BCG corrected and AAS BCG corrected data, two lowest rows of electrodes around the neck and face (69 electrodes) and ECG electrode were removed keeping 187 electrodes for further analysis (Supplementary Figure S3). On the remaining 187 electrodes, noisy and bad electrodes, which were identified when the *SD* of the normalized time-course of each electrode exceeded 5 *SD* (Delorme & Makeig, 2004; Uji, Jentsch, Redburn, & Vishwanath, 2019), were removed and interpolated using neighbour electrodes. Resulting data were then further downsampled into 250 Hz and re-referenced to an average of all non-noisy channels, using EEGLAB software (<https://scn.ucsd.edu/eeqlab>) (Delorme & Makeig, 2004). After common average reference, all timepoints before and after the MRI scanning were removed, and further analyses were conducted on EEG data specifically during the MRI scanning.

2.5.1 | EEG beamforming

To examine how the beamforming technique would attenuate BCG artefacts and preserve task-induced brain signals, we considered a linearly constrained minimum variance (LCMV) beamforming analysis (Brookes, Mullinger, et al., 2008; Uji et al., 2018; van Veen et al., 1997), using Fieldtrip toolbox (Fieldtrip-20191014, <http://www.ru.nl/neuroimaging/fieldtrip>) (Oostenveld, Fries, Maris, & Schoffelen, 2011).

EEG electrode locations were first accurately digitized using the EGI GPS to facilitate individualized co-registration of electrode positions with each subject's anatomical image (Russell et al., 2005). The digitized EEG electrode positions were co-registered with the subjects' T1-weighted anatomical image using fiducials and scalp surface fitting. A four-layer (scalp, skull, cerebrospinal fluid [CSF], and brain), anatomically realistic volume conduction boundary element model

(BEM) (Fuchs, Kastner, Wagner, Hawes, & Ebersole, 2002; Oostendorp & van Oosterom, 1991) was created by segmenting each subject's T1-weighted images into skin, skull, CSF, and brain compartments. In the four-layer BEM head model, the electrical conductivity of the scalp, the skull, CSF, and the brain was set to 0.33, 0.0042, 1 and 0.33 S/m, respectively (Gramfort, Papadopoulos, Olivi, & Clerc, 2010; Kybic, Clerc, Faugeras, Keriven, & Papadopoulos, 2006). A template grid (5 mm spacing) covering the whole brain volume was created from the MNI template brain (Colin27) and transformed to each subject's anatomical space. The lead-field matrix at each location on the template grid in individual subject space was then calculated using their BEM, not constraining the orientation of the dipolar source placed on that point of the grid (Sekihara et al., 2004). The full details of mathematical information behind the beamforming spatial filtering technique can be found in the previous article (van Veen et al., 1997).

Using the LCMV beamforming spatial filtering, an estimate of the source amplitude vector $\hat{Q}(r, t)$ at source space location, r , and time, t , is made using a weighted sum of the electrical measurements recorded at each of the n electrodes such that:

$$\hat{Q}(r, t) = W(r)^T V(t) \quad (1)$$

where $V(t)$ is an n -dimensional column vector of electric potential measurements made at time t , and $W(r)$ is a $3 \times n$ matrix of weighting parameters that are tuned specifically to the location r . Superscript T indicates a matrix transpose. The weighting parameters are calculated such that they minimize the total variance in the output signal $\hat{Q}(r, t)$, which will result in minimizing the influence of signals originated from any other location than the one of interest in r , while maintaining a constraint that any activity originating at the specific location r must remain in $\hat{Q}(r, t)$.

$$\min_{W(r)} \left[\varepsilon \left(\left\| \hat{Q} \right\|^2 \right) \right] \text{ subject to } W(r)^T L(r) = I \quad (2)$$

$$\min_{W(r)} \left[W(r)^T (C + \lambda I) W(r) \right] \text{ subject to } W(r)^T L(r) = I \quad (3)$$

$$W(r)^T = \left[L(r)^T \{C + \lambda I\}^{-1} L(r) \right]^{-1} L(r)^T \{C + \lambda I\}^{-1} \quad (4)$$

where $L(r)$ represents a $3 \times n$ matrix in which the first, second and third columns of the lead field matrix for the position r , consisting of the electrical fields that would be measured at each of the n electrodes in response to a source of unit amplitude sited at location r and orientated in the x , y , and z directions respectively. $L(r)$ was therefore based on an EEG forward solution, (Sekihara et al., 2004; van Veen et al., 1997). ε denotes the mathematical expectation, whereas the matrix I represents the identity matrix. Here, $C = \varepsilon(V(t)V(t)^T)$ representing the $n \times n$ data covariance matrix calculated over a time-frequency window of interest using the entire epoched trials after removing noisy trials contaminated with large motion artefacts. λ is a regularization parameter and the regularized covariate matrix was calculated as $(C + \lambda I)$. By the reducing the regularization parameters

it is possible to make the beamforming filter more spatially selective (Brookes, Vrba, et al., 2008), and this would result in substantial suppression of the artefact (Litvak et al., 2010). Therefore, especially in the context of EEG–fMRI, a small regularization parameter of 0.01% is recommended to be used, therefore allowing more artefact suppressions (Brookes, Vrba, et al., 2008; Litvak et al., 2010).

Both non-BCG corrected and AAS BCG corrected data were epoched from -2 to 3 s relative to the probe cue events for identifying the alpha ERD VE location in the visual region (visual epoched data), and epoched from -4 to 2 s relative to the movement onsets for the beta ERD VE location in the motor region (movement epoched data). To achieve cleaner EEG data, around 5–10% trial rejection rate is usually recommended (Delorme, Sejnowski, & Makeig, 2007), and by applying amplitude threshold of $\pm 500 \mu\text{V}$ on the AAS BCG corrected data, noisy EEG trials, that were contaminated with large motion artefacts, were detected and removed (Delorme et al., 2007; Uji et al., 2019). This resulted in a group mean ($\pm SD$) number of remaining trials of 132 ± 7 trials for each run for the visual epoched trials and 117 ± 15 trials for each run for the movement epoched trials for further analysis. The same numbers of trials were used for both AAS BCG corrected and non-BCG corrected data analysis.

In order to improve SNRs of the beamforming spatial filtering, an optimum source orientation/direction needs to be calculated instead of using 3D vector (x, y, z) at the source space location r (Sekihara et al., 2004). The optimal orientation $\text{opt}(r)$ at the position r can be computed by the eigenvector corresponding to the minimum generalized eigenvalue of the matrix $[L(r)^T(C + \lambda I)^{-2}L(r)]$ with the metric $[L(r)^T(C + \lambda I)^{-1}L(r)]$ (Sekihara et al., 2004; Sekihara & Nagarajan, 2008). Once $\text{opt}(r)$ is obtained, the beamforming weight vector (1D vector) can be calculated.

A scalar LCMV beamforming (Sekihara et al., 2004; Sekihara & Nagarajan, 2008) with individual BEM head models using the regularization parameter of 0.01% (Brookes, Vrba, et al., 2008; Litvak et al., 2010) was carried out for each subject to calculate beamforming weights (weights of each EEG channel at each lead-field virtual electrode [VE] position r in the brain) derived from the entire broadband data (1–100 Hz) and a covariance matrix calculated using the entire clean dataset of either visual or movement epoched trials after removing noisy trials (Brookes, Mullinger, et al., 2008). For every VE location within the source grid space, the estimated VE trial time-courses were then band-pass filtered using sixth-order Butterworth filters in the frequency band of interest (alpha: 8–13 Hz; beta: 13–30 Hz).

To identify the VE locations of interest, related to the induced task neural activity, that is, visual alpha ERD and motor beta ERD, a pseudo-T statistic can be calculated by the following:

$$T = \frac{\hat{Q}(r)^2 - \hat{v}(r)^2}{\hat{Q}(r)^2 + \hat{v}(r)^2} \quad (5)$$

where $\hat{Q}(r)^2$ represents the beamformer power estimated in r during an active time window, whereas $\hat{v}(r)^2$ represents the beamformer power estimated in r during a control baseline time window (Brookes, Mullinger, et al., 2008; Hillebrand & Barnes, 2005; Robinson & Vrba, 1999).

Specifically, to detect the alpha ERD VE location following visual stimuli, we calculated alpha power during the active time window of 0.1–1.1 s after the probe cues, and the baseline period was defined between -1.5 and -0.5 s prior to the probe cues. We then identified the minimum peak of the pseudo-T statistic map reflecting the largest alpha band power decrease, as the alpha VE location for each subject. To detect the beta ERD VE location during movement preparation/planning, we calculated beta power during the active time window between -1.25 and -0.25 s prior to the movement onsets, whereas the baseline time window was defined between -3.0 and -2.0 s prior to the movement onsets. We then identified the minimum peak of the pseudo-T map reflecting the largest beta band power decrease, as the beta VE location in the brain for each subject. From these pseudo-T maps, VE locations were separately identified for each subject. The alpha ERD VE location was indeed detected in the visual cortex (visual alpha VE) from the visual epoched data, whereas the beta ERD VE location was identified in the motor cortex (motor beta VE) from the movement epoched data.

A broadband (1–100 Hz) time-course of neural activity during the whole MRI scanning period was then also calculated from these two subject-specific VE locations, using Equation (1). The beamforming weights of the visual alpha VE and motor beta VE were applied to the entire time-course of the whole 187 scalp electrodes during MRI scanning for R-peak locked analysis and ANT task-based analysis.

For further event-locked analysis, namely R-peak locked analysis and then ANT task-based analysis, we considered four data sets (non-BCG corrected; AAS BCG corrected; beamforming BCG corrected; beamforming + AAS BCG corrected) consisting of non-BCG corrected and AAS BCG corrected sensor level data and broadband (1–100 Hz) source level time-courses in the visual and motor beamforming VEs estimated from either non-BCG corrected or AAS BCG corrected data.

2.5.2 | R-peak locked analysis

Sensor-level analysis

To investigate the effects of BCG artefacts on the EEG data at the sensor level, both non-BCG corrected and AAS BCG corrected data were epoched from -5 to 5 s relative to every detected R-peak event (group mean number [$\pm SD$] of R-peak events for each run = 870 ± 126 events). Two main analyses were conducted: (a) R-peak locked time-course analysis and (b) R-peak locked time–frequency analysis.

For the R-peak locked time-course analysis, each R-peak locked time-course for each electrode was extracted, and each 10s epoch was demeaned by subtracting the mean value of the 10s epoch and divided by the *SD* of the 10s epoch for normalized z-score transformation, for each selected epoch. This z-score transformation allowed us to make comparisons in the same scale since there would be differences in the amplitudes and SNR in the sensor and source level signals. Then, calculated z scores were averaged across epochs first and then across subjects, for each electrode in both non-BCG corrected and AAS BCG corrected data.

In the R-peak locked time–frequency analysis, time–frequency spectrograms of each 10s epoch for each channel were calculated using a multitaper approach (Scheeringa et al., 2011; Uji et al., 2018) using the Fieldtrip toolbox. Windows of 0.8 s duration were moved across the data in steps of 50 ms, resulting in a frequency resolution of 1.25 Hz, and the use of three tapers resulted in a spectral smoothing of ± 2.5 Hz. The calculated time–frequency representations (TFRs) were then transformed in the scale of dB by $10 \cdot \log_{10}$, then demeaned by subtracting the mean power in each frequency during the 10s epoch to calculate power fluctuations around a single R-peak, and averaged across epochs first and then across subjects for each electrode in both non-BCG corrected and AAS BCG corrected data.

Source-level analysis

The same R-peak locked time-course analysis and time–frequency analysis was conducted on the beamforming estimated time-course signals from the AAS BCG corrected (beamforming + AAS BCG corrected) and non-BCG corrected (beamforming BCG corrected) data. The whole time-course signals during the MRI scanning were estimated from the two VE locations using Equation (1). We then epoched the whole visual VE and motor VE signals from -5 to 5 s relative to every R-peak event from the AAS BCG corrected data. Both R-peak locked time-courses and TFRs were averaged across epochs and then across subjects for both VE locations estimated from both the AAS BCG corrected (beamforming + AAS BCG corrected) and non-BCG corrected data (beamforming BCG corrected).

2.5.3 | ANT task-based analysis

The time–frequency analysis was chosen to investigate the effects of the BCG artefacts in the time–frequency domains, which normally obscure the EEG signals below 20 Hz. This analysis was conducted on both visual and movement epoched data separately for both non-BCG corrected and AAS BCG corrected data. In the sensor space, using the same multitaper approach described above, we calculated the TFRs in the visual epoched data for each channel, and the time–frequency spectrograms were converted to display power change in the task-induced neural activity relative to baseline in the scale of dB ($10 \cdot \log_{10}[\text{signal}/\text{baseline}]$) with the baseline period between -1.5 and -0.5 s prior to the probe cues. For the movement epoched data, the same analysis was conducted using the baseline period between -3.0 and -2.0 s prior to the movement onsets.

In the source-space analysis, both visual and movement epoched trial time-courses were estimated from the two VE locations using Equation (1) with respective beamforming spatial filter and epoched EEG signals from the AAS BCG corrected and non-BCG corrected data. The same time–frequency analysis was conducted for the visual alpha VE signals using the baseline period between -1.5 and -0.5 s prior to the probe cues, whereas the motor beta VE signals were analysed using the baseline period between -3.0 and -2.0 s prior to the movement onsets in the same time–frequency analysis.

2.5.4 | Statistical analysis

Non-parametric cluster-based permutation tests (Fieldtrip) (Maris, 2012; Maris & Oostenveld, 2007; Nichols & Holmes, 2002) were used to examine significant differences comparing the absolute power of TFRs in the sensor and source space from the R-peak locked and ANT task-based analysis. To do so, when comparing two BCG correction strategies among the four proposed investigations (e.g., beamforming + AAS BCG corrected vs. AAS BCG corrected), we considered all normalized TFR maps from all 20 subjects to build a time–frequency t-map of the difference between the two approaches, therefore taking into account inter-subject variability. For each combination of methods to be tested, statistical inference was based on a non-parametric cluster-based permutation test, which resulted in time–frequency t-map clusters obtained when first applying a threshold of alpha level of .001. From this thresholded time–frequency t-map, the t-values were summed per cluster and then used as the test statistic. A randomization distribution of this test statistic was determined by randomly exchanging 1,000 times, through permuting the two conditions among the $N = 20$ subjects and the permutation p -value of the cluster of interest was approximated by a Monte Carlo estimate. This was done by building a null distribution considering all possible permutations given the number of subjects ($N = 20$), and for each randomization only the maximal test statistic was retained. An observed cluster was deemed significant if it fell outside the central 95% of this randomization null distribution, corresponding to a two-sided random effect test with 5% false positives, corrected for the multiple comparisons across times and frequencies. The significant spectral-temporal cluster masked the raw TFR difference. The permutation test has advantages over the Bonferroni correction for multiple comparisons because the Bonferroni correction assumes that all measures are independent, an assumption that is too strong and weakens the power of the statistical test. In contrast, the permutation test considers the true dependency among all of the measures. Additionally, if there were any significant clusters, effect sizes in the TFRs were calculated by mean difference divided by the SD using Cohen's d (Cohen, 1988; Gross et al., 2013; Sawilowsky, 2009). Then, the Cohen's d values were averaged within the significant cluster to estimate the effect size of the cluster-based permutation test (Cohen, 1962, 1988; Sawilowsky, 2009). Based on Sawilowsky (2009), the effect size can be categorized as $d(0.01) = \text{very small}$, $d(0.2) = \text{small}$, $d(0.5) = \text{medium}$, $d(0.8) = \text{large}$, $d(1.2) = \text{very large}$, and $d(2.0) = \text{huge}$, and the effect sizes are directional having positive and negative in terms of the direction of the comparison (Cohen, 1962).

2.5.5 | SNR comparisons during ANT

$$\text{SNR} = \frac{\left| \text{Mean}\left(\text{TFR}\left[\hat{Q}(r)\right]\right) - \text{Mean}\left(\text{TFR}\left[\hat{p}(r)\right]\right) \right|}{\text{std}\left(\text{TFR}\left[\hat{p}(r)\right]\right)} \quad (6)$$

where $\text{TFR}\left[\hat{Q}(r)\right]$ denotes the time–frequency power at either EEG electrode or VE location of interest, within the frequency range of

interest during the active time window, whereas $TFR[\hat{v}(r)]$ represents the time–frequency power at either EEG electrode or VE location of interest, within the frequency range of interest during the control baseline time window. *Mean* and *std* denotes, respectively, the mean and SD computed over all coefficients of the selected time–frequency area.

Since the alpha and beta ERD exhibits power reduction when compared to the baseline, SNRs at the sensor and source levels were calculated as the absolute value of the difference. Then, group mean SNR value was calculated by averaging SNR value across all trials first and then across subjects as suggested in Hill et al. (2020), for each electrode (non-BCG corrected; AAS BCG corrected) and each VE location (beamforming + AAS BCG corrected; beamforming BCG corrected). The active and control baseline time windows were consistent throughout the data analysis. For the visual alpha (8–13 Hz) ERD, the active window was the time period between 0.1 and 1.1 s as compared with the baseline window of -1.5 to -0.5 s relative to the probe cue onset, whereas for the motor beta (13–30 Hz) ERD, the active window was the time period between -1.25 and -0.25 s as compared with the baseline window of -3 to -2 s relative to the movement onset.

3 | RESULTS

3.1 | BCG artefact attenuation

3.1.1 | BCG artefact corrections in the sensor space

The group mean R-peak locked time-courses from the non-BCG corrected data were represented on 17 electrodes selected from the

EGI geodesic electrodes, which have the equivalent locations from the international 10–20 EEG system (see Figure 2). The group mean R-peak locked time-courses from the AAS BCG corrected data on the same 17 electrodes, are represented in Figure 3. The fluctuations of the non-BCG artefact time-courses resulted in z-scores values ranging between 0.5 and 1 at the time of R-peaks (Figure 2). When considering the resulting residual BCG artefact after applying the standard AAS correction method, we obtained peak z-score values ranging between 0.05 and 0.1 (Figure 3), demonstrating that the conventional AAS approach enabled around 10-fold improvement in the suppression of BCG artefacts.

The group mean TFRs time-locked at the individual R-peak events, when applied on non-BCG corrected data, are presented in Figure 4 on the selected 17 electrodes. The group mean TFRs time-locked at the individual R-peak events from the AAS BCG corrected data, are presented in Figure 5. When considering non-BCG corrected data, the power fluctuations of the BCG artefact were observed at the peak power of around 1 dB, especially below 20 Hz, at the time of R-peaks (Figure 4). After applying the standard AAS BCG correction, these power fluctuations were reduced to the peak power of around 0.2 dB at the time of R-peaks especially below 20 Hz (Figure 5). In Figure 6, the cluster-based permutation tests revealed significant differences ($p < .05$) between the AAS BCG corrected and non-BCG corrected data for all the selected 17 electrodes, confirming that the standard AAS technique removed the BCG artefacts significantly. The effect sizes of the cluster-based permutation tests on the sensor level were ranged from $d = 1.11$ to $d = 1.18$, which revealed the large effect (Figure 6). Although some of the residual artefacts can still be observed above 20 Hz, the AAS method, in general,

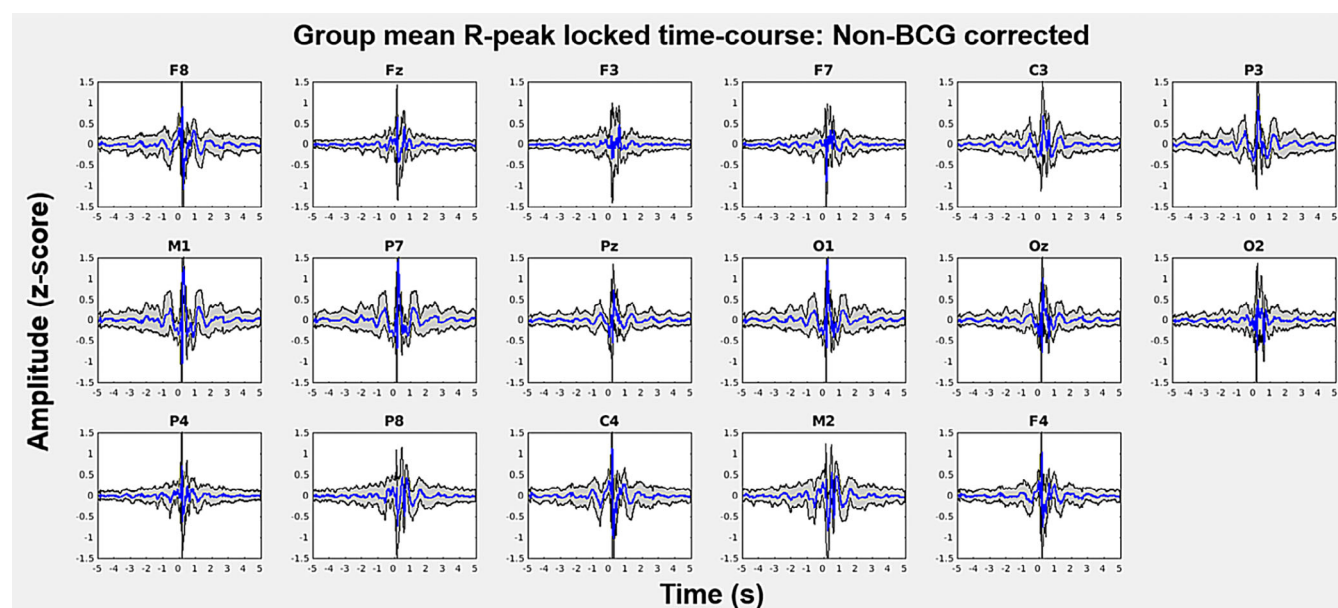


FIGURE 2 Group mean \pm SD ($N = 20$ participants) z-scores of ballistocardiogram (BCG) artefact related time-courses time-locked at individual R-peak events from electrocardiography (ECG) recording during each run (three runs of 13 min in total). The time-courses were measured from no BCG corrected data on 17 electrodes selected from an Electrical Geodesics Inc (EGI) geodesic 256 electroencephalography (EEG) system. Specifically, E2 (F8), E21 (Fz), E36 (F3), E47 (F7), E59 (C3), E87 (P3), E94 (M1), E96 (P7), E101 (Pz), E116 (O1), E126 (Oz), E150 (O2), E153 (P4), E170 (P8), E183 (C4), E190 (M2), and E224 (F4) electrodes have the equivalent locations in an international 10–20 EEG system from the EGI geodesic 256 EEG system. It needs to be noted that the scales of y-axis at the sensor level are within ± 1.5 z-scores

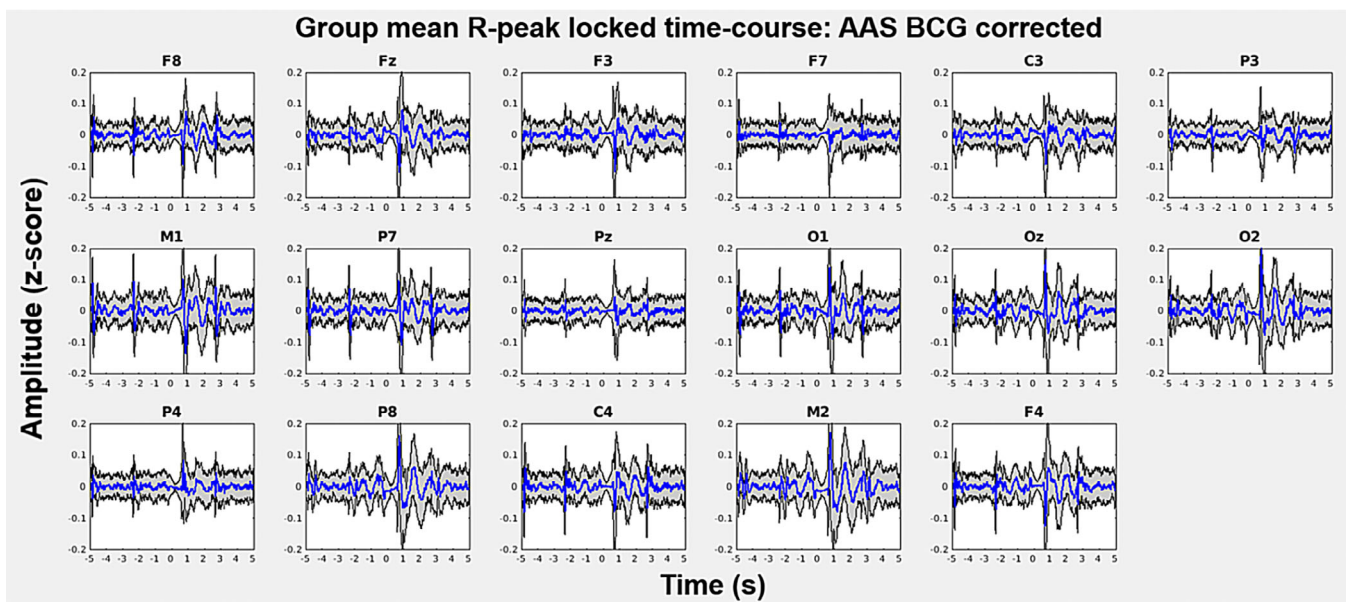


FIGURE 3 Group mean \pm SD ($N = 20$ participants) z-scores of ballistocardiogram (BCG) artefact corrected time-courses time-locked at individual R-peak events from electrocardiography (ECG) recording during each run (three runs in total). The time-courses were measured from the BCG corrected data (average artefact subtraction [AAS] approach) on 17 electrodes selected from an Electrical Geodesics Inc (EGI) geodesic 256 electroencephalography (EEG) system. Specifically, E2 (F8), E21 (Fz), E36 (F3), E47 (F7), E59 (C3), E87 (P3), E94 (M1), E96 (P7), E101 (Pz), E116 (O1), E126 (Oz), E150 (O2), E153 (P4), E170 (P8), E183 (C4), E190 (M2), and E224 (F4) electrodes have the equivalent locations in an international 10–20 EEG system from EGI geodesic 256 EEG system. It needs to be noted that after the AAS BCG corrections, the scales of y-axis at the sensor level are within ± 0.2 z-scores

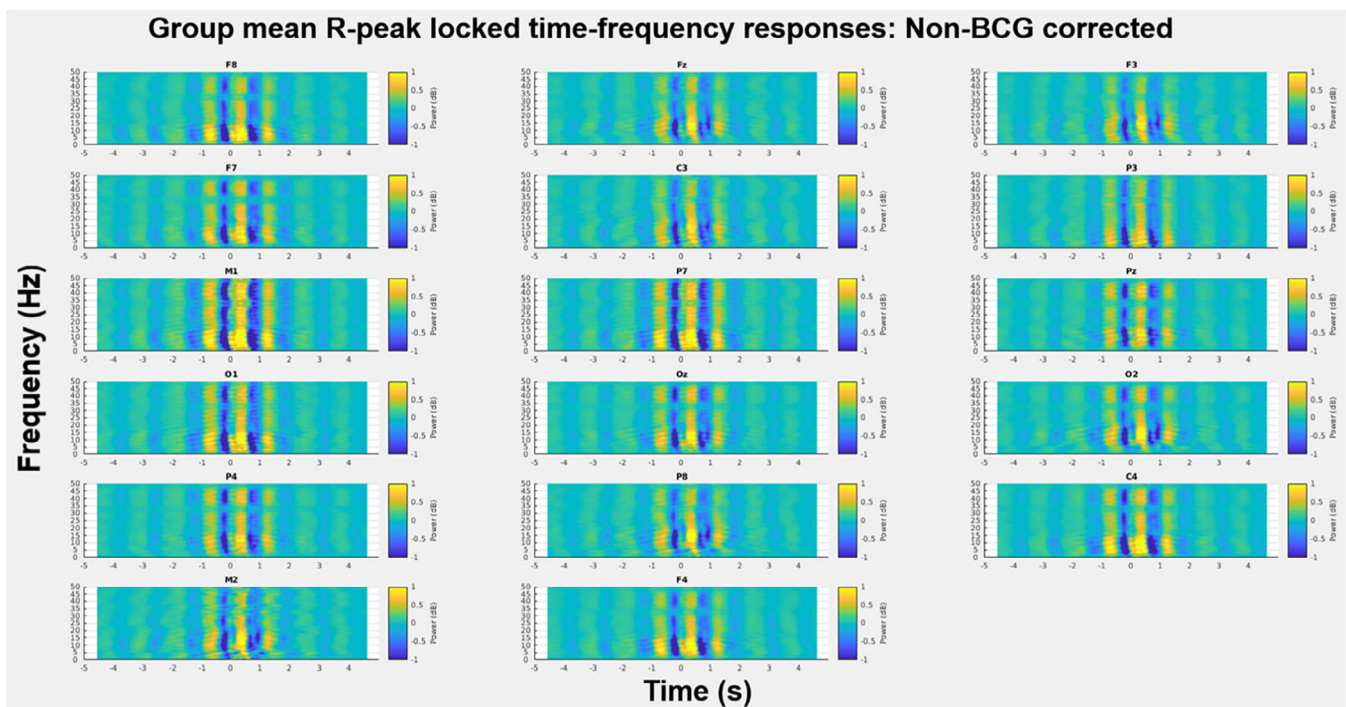


FIGURE 4 Group mean ($N = 20$) time–frequency representations (TFRs) of ballistocardiogram (BCG) artefact related signals time-locked at individual R-peak events from electrocardiography (ECG) recording during each run (three runs in total). The TFRs were calculated from non-BCG corrected data on selected 17 electrodes from an Electrical Geodesics Inc (EGI) geodesic 256 electroencephalography (EEG) system. Specifically, E2 (F8), E21 (Fz), E36 (F3), E47 (F7), E59 (C3), E87 (P3), E94 (M1), E96 (P7), E101 (Pz), E116 (O1), E126 (Oz), E150 (O2), E153 (P4), E170 (P8), E183 (C4), E190 (M2), and E224 (F4) electrodes have the equivalent locations in an international 10–20 EEG system from EGI geodesic 256 EEG system. It needs to be noted that the scales of colour bars in this figure are within ± 1 dB

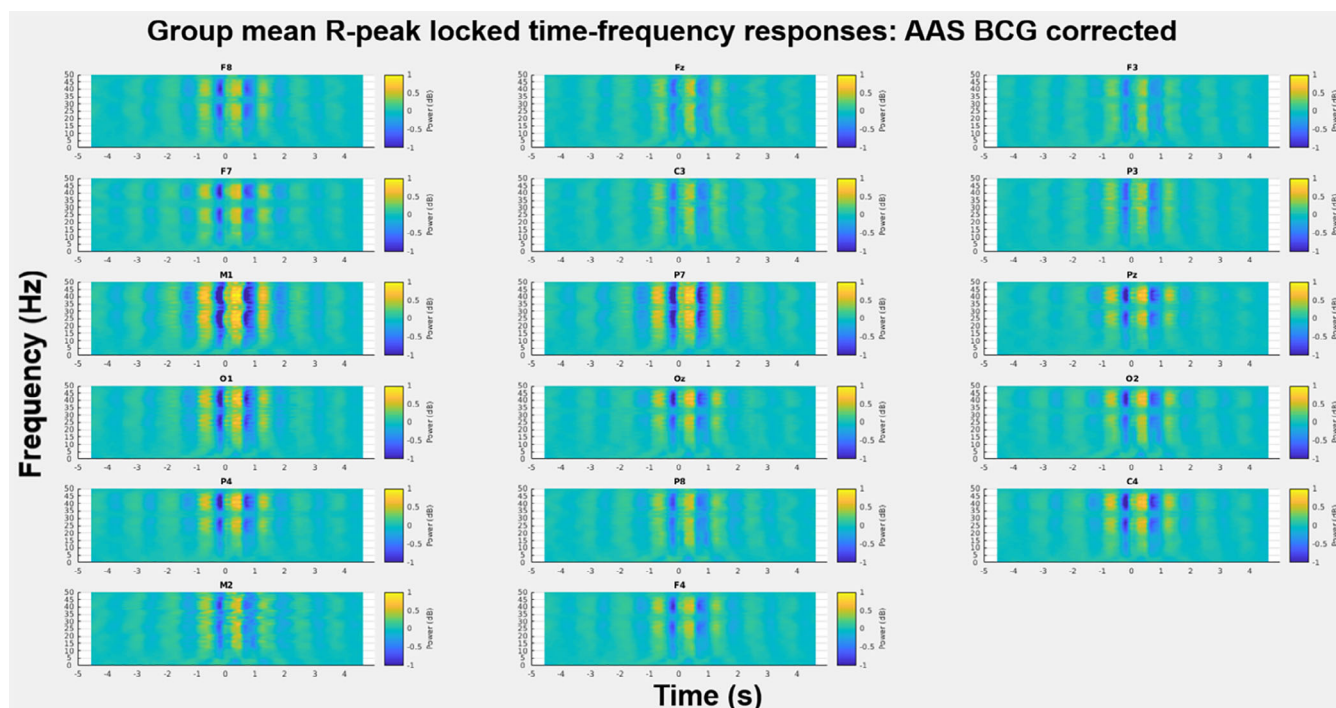


FIGURE 5 Group mean ($N = 20$) time–frequency representations (TFRs) of ballistocardiogram (BCG) artefact corrected signals time-locked at individual R-peak events from electrocardiography (ECG) recording during each run (three runs in total). The TFRs were calculated from the BCG corrected data (average artefact subtraction [AAS] approach) on selected 17 electrodes from an Electrical Geodesics Inc (EGI) geodesic 256 electroencephalography (EEG) system. Specifically, E2 (F8), E21 (Fz), E36 (F3), E47 (F7), E59 (C3), E87 (P3), E94 (M1), E96 (P7), E101 (Pz), E116 (O1), E126 (Oz), E150 (O2), E153 (P4), E170 (P8), E183 (C4), E190 (M2), and E224 (F4) electrodes have the equivalent locations in an international 10–20 EEG system from EGI geodesic 256 EEG system. It needs to be noted that the scales of colour bars in this figure are within ± 1 dB

demonstrated overall good suppression of BCG artefacts in time–frequency domains by comparing the TFRs of the non-BCG corrected and AAS BCG corrected data.

3.1.2 | Beamforming approach

Figure 7 (left column) shows the group average T-statistic map of alpha power changes during the active time-window (0.1–1.1 s after the probe cue onset) compared to the baseline time-window (–1.5 to –0.5 s prior to the probe cue onset) from the BCG corrected and non-BCG corrected data. Alpha power decrease (ERD, negative T values) was observed in the visual cortex in both beamforming + AAS BCG corrected and beamforming BCG corrected datasets. Figure 7 (right column) shows the group average T-statistic map of beta power changes during the active time-window (–1.25 to –0.25 s before the movement onset) compared to the baseline time-window (–3 to –2 s prior to the movement onset) from the beamforming + AAS BCG corrected and beamforming BCG corrected data. Beta power decrease (ERD, negative T values) was observed in the motor cortex in both data set. Based on the pseudo-T statistic map (Figure 7, cross-hairs), the MNI coordinates of the group mean visual alpha VE location ($\pm SE$) was $[-25 \pm 4, -75 \pm 1, -8 \pm 3]$ mm [MNI:x,y,z] for the AAS BCG corrected data and $[2 \pm 4, -96 \pm 1, 9 \pm 3]$ mm [MNI:x,y,z] for the non-BCG corrected data. The MNI coordinates of the group mean

motor beta VE location ($\pm SE$) was $[45 \pm 5, -44 \pm 3, 54 \pm 2]$ mm [MNI:x,y,z] for the AAS BCG corrected data and $[55 \pm 7, -35 \pm 3, 50 \pm 2]$ mm [MNI:x,y,z] for the non-BCG corrected data.

The group mean VE time-courses time-locked at the individual R-peak events were also calculated from the AAS BCG artefact corrected data in Figure 8. It is important to mention that the fluctuations of the remaining BCG artefact on the VE time-courses from the beamforming BCG corrected data, resulted in the peak z-score values around 0.05 (Figure 8), when compared to the original BCG artefacts which had the peak z-scores between 0.5 and 1 at the R-peak events in the sensor space of the non-BCG corrected data (Figure 2). Moreover, the fluctuations of the remaining BCG artefact from the beamforming BCG corrected data was similar to those of the - beamforming + AAS BCG corrected data showing the peak z-score values around 0.05 (Figure 8), suggesting that whether or not the AAS was considered at the sensor level, spatial filtering using beamforming was able to reach the similar amount of BCG artefact removal.

The power fluctuations of the remaining BCG artefact from the VE signals of the non-BCG corrected data were observed at the peak power of around 0.2 dB at the time of R-peaks (Figure 8), resulting in a large attenuation of the BCG artefacts which were originally exhibiting a peak power of around 1 dB at the R-peak events, especially below 20 Hz (Figure 3). In Figure 9b, the cluster-based permutation tests revealed significant reduction ($p < .05$) of the BCG artefact between the beamforming BCG corrected data (visual alpha VE,

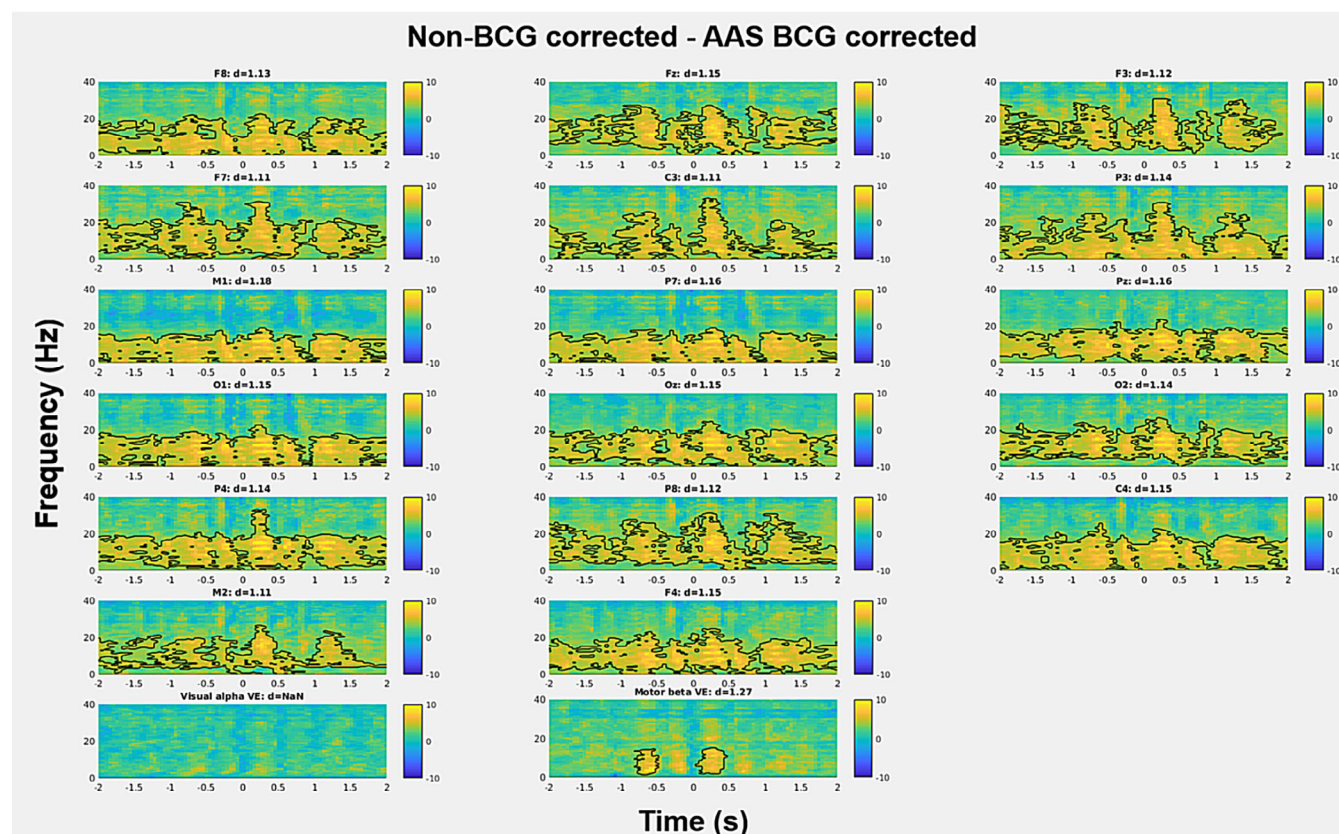


FIGURE 6 The t-maps of differences in the time–frequency representations (TFRs) between the average artefact subtraction (AAS) ballistocardiogram (BCG) corrected and non-BCG corrected data in both sensor and source levels (visual and motor virtual electrodes (VEs)). Figures demonstrate t-values (“non-BCG corrected” minus “AAS BCG corrected”) and black contour representing the significant clusters from cluster-based permutation tests ($p < .05$), and if there is a significant cluster, Cohen's d is calculated as the effect size. Yellow denotes a positive t-value showing greater power in the non-BCG corrected data when compared to the AAS BCG corrected data, whereas blue denotes a negative t-value revealing greater power in the AAS BCG corrected data when compared to the non-BCG corrected data. The figures indicate a significant reduction of the BCG artefacts when applying AAS, as opposed to non-BCG correction, and overall significant improvement of AAS method for signals below 20 Hz

motor beta VE) and corresponding non-BCG corrected electrodes (Oz, C4), confirming that the beamforming technique significantly removed the BCG artefacts, even from non-corrected data.

By comparing the standard AAS approach (AAS BCG corrected data) and beamforming + AAS BCG corrected data (Figure 9a), the cluster-based permutation tests revealed significant differences ($p < .05$) between the beamforming + AAS BCG corrected data (visual alpha VE, motor beta VE) and corresponding AAS BCG corrected electrodes (Oz, C4), suggesting the beamforming spatial filtering could also further improve the BCG artefact suppressions even after the standard AAS approach in the sensor space. Furthermore, the cluster-based permutation tests (Figure 9c) revealed significant differences ($p < .05$) between the beamforming BCG corrected data (visual alpha VE, motor beta VE) and corresponding AAS BCG corrected electrodes (Oz, C4), demonstrating that the performance of this beamforming BCG denoising for the non-BCG corrected data (Figure 8) was significantly greater than the level of the conventional AAS approach (Figure 5). This finding indicates that the proposed data-driven beamforming denoising approach allows significantly attenuating the BCG artefacts without relying on R-peak detections from ECG recording. Finally, by comparing the performance

of both beamforming approaches (beamforming + AAS BCG corrected, beamforming BCG corrected), the permutation tests revealed that the beamforming + AAS BCG corrected data contained significantly less BCG artefacts than the beamforming BCG corrected data in the motor beta VE ($p < .05$), although there was no significant difference between them in the visual alpha VE, indicating some advantages of applying the beamforming technique on the corrected data, when compared to solely applying beamforming on the uncorrected data (Figure 6). The effect sizes of the significant clusters were ranged from $d = 1.05$ to $d = 1.17$, which revealed the large effect (Figures 6 and 9).

3.2 | ANT task activity

3.2.1 | Visual alpha ERD

Analysis at the sensor level

Figure 10 shows the group mean TFRs measured in selected occipital and parietal electrodes, reporting alpha (8–13 Hz) power change in response to the target cues which occurred at 600 ms after the probe

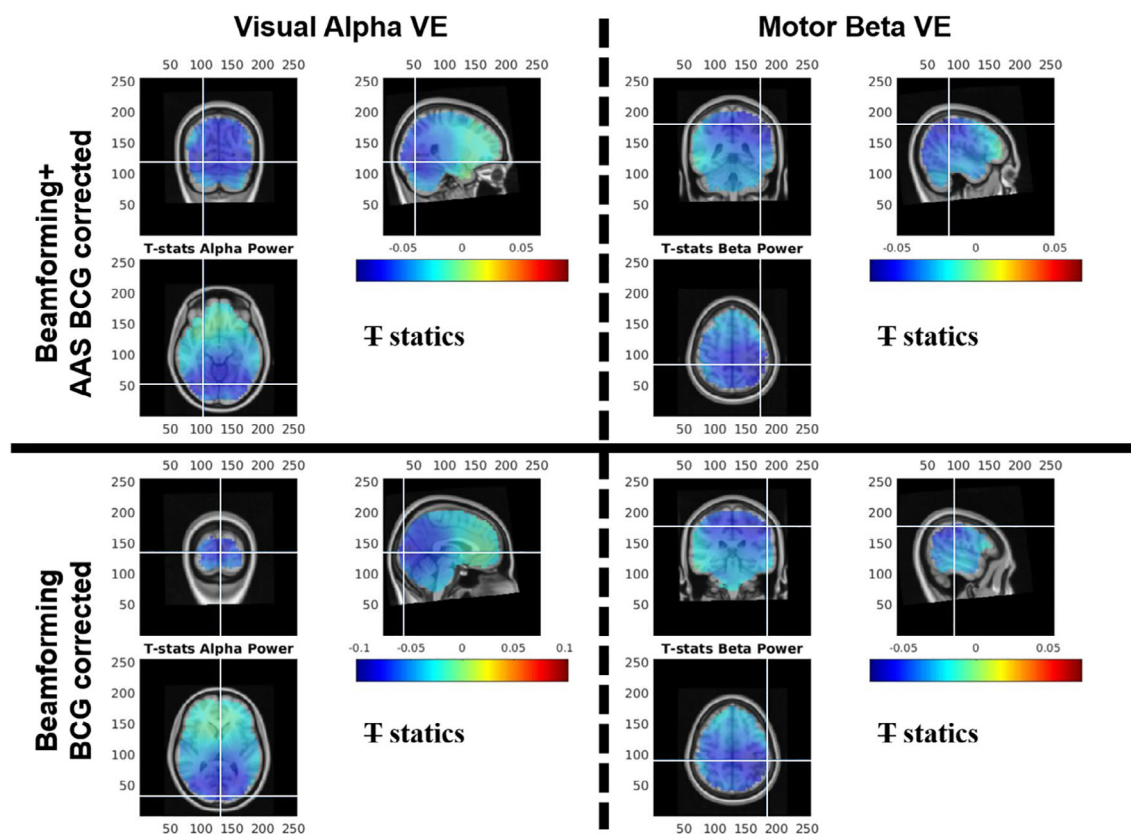


FIGURE 7 Group average ($N = 20$) pseudo-T statistic beamforming maps showing (left column) regions exhibiting power decreases in alpha frequency (8–13 Hz) during the active window (0.1–1.1 s) as compared with the baseline window (–1.5 to –0.5 s) relative to the probe cue onset from the average artefact subtraction (AAS) ballistocardiogram (BCG) corrected (top) and non-BCG corrected data (bottom), whereas (right column) regions exhibiting power decrease in beta frequency (13–30 Hz) during the active window (–1.25 to –0.25 s) as compared with the baseline window (–3 to –2 s) relative to the movement onset from the AAS BCG corrected (top) and non-BCG corrected data (bottom). The crosshairs represent the group average of the individual virtual electrode (VE) locations found in visual cortex for the alpha frequency activity (left column) and in the motor cortex for the beta frequency activity (right column). The group mean visual alpha VE locations across subjects ($\pm SE$) was found at $[-25 \pm 4, -75 \pm 1, -8 \pm 3]$ mm [MNI:x,y,z] for the beamforming + AAS BCG corrected data and $[2 \pm 4, -96 \pm 1, 9 \pm 3]$ mm [MNI:x,y,z] for the beamforming BCG corrected data (see crosshairs), whereas the group mean motor beta VE locations ($\pm SE$) was found at $[45 \pm 5, -44 \pm 3, 54 \pm 2]$ mm [MNI:x,y,z] for the beamforming + AAS BCG corrected data and $[55 \pm 7, -35 \pm 3, 50 \pm 2]$ mm [MNI:x,y,z] for the beamforming BCG corrected data, both of which were contralateral to the left hand button presses (see crosshairs)

cue onset (either no cue, double cue, or spatial cue). Results are reported when considering results obtained for the AAS BCG corrected data (top row) and non-BCG corrected data (bottom row). Despite the large broadband increases in power (red vertical stripes occurred after around 1 s in response to the probe cue onset) demonstrated the motion artefacts caused by the button press for the task responses (see Supplementary Figure S4), alpha power decrease (alpha ERD) was still observed within the time window before 1 s when compared to baseline time-window (–1.5 to –0.5 s prior to the probe cue onset) in the AAS BCG corrected data (see top row in Figure 10). However, this alpha ERD was difficult to identify in the same electrodes from the non-BCG corrected data (see bottom row in Figure 10) as the alpha power within the active time-window (0.1–1.1 s after the probe cue onset) was reduced from -0.91 ± 0.45 dB (AAS BCG corrected data) to -0.71 ± 0.29 dB (non-BCG corrected data) in the Oz electrode, revealing that the BCG artefacts, which are typically below 20 Hz, masked the alpha power change related to the

visual stimuli. In Figure 11, the cluster-based permutation tests demonstrated significant differences ($p < .05$) between the AAS BCG corrected and non-BCG corrected data in the occipital electrodes (O1, Oz, O2), confirming that the visual alpha ERD can be observed at the occipital electrodes in the standard AAS BCG corrected data, when compared to the non-BCG corrected data at the sensor level. Furthermore, the significant clusters revealed the large to very large effect sizes ranged from $d = 1.11$ to $d = 1.24$ (Figure 11).

Beamforming source reconstructions

Figure 14 (left column) shows the group average TFRs measured in the visual alpha VE for alpha (8–13 Hz) power change in response to the target cues which occurred at 600 ms after the probe cue onset (either no cue, double cue, or spatial cue) from the AAS BCG corrected data (top row) and non-BCG corrected data (bottom row). Although the broadband increases in power (red vertical stripes occurred after around 1 s in response to the probe cue onset) was

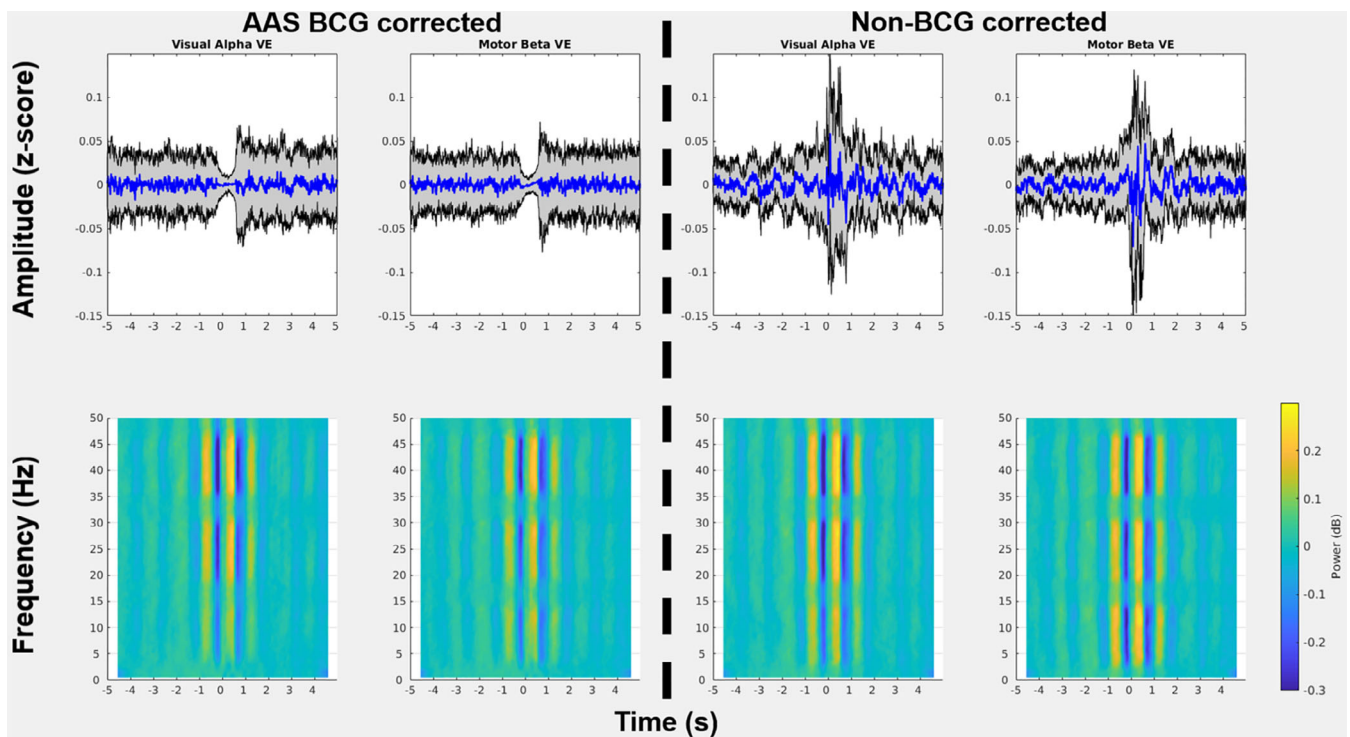


FIGURE 8 Group mean ($N = 20$) time-courses ($\pm SD$) and time-frequency representations (TFRs) of ballistocardiogram (BCG) artefact related signals time-locked at individual R-peak events from two virtual electrodes (VEs) in the visual and motor cortex after applying beamforming techniques on either average artefact subtraction (AAS) BCG corrected (beamforming + AAS BCG corrected) or non-BCG corrected data (beamforming BCG corrected). It needs to be noted that the scales of the y-axis in the time-course amplitude are within ± 0.15 z-scores, whereas those of the colour bars in the TFR are within ± 0.3 dB

caused by motion artefacts occurring at the time of the button press for the task responses, alpha power decrease (alpha ERD) was observed within the time window before 1 s as compared to baseline time-window (-1.5 to -0.5 s prior to the probe cue onset) in both AAS BCG corrected and non-BCG corrected data (see left column in Figure 14). The alpha ERD within the active time-window (0.1 – 1.1 s after the probe cue onset) from the BCG corrected data was -1.26 ± 0.48 dB with the peak alpha frequency of 11 Hz (see top row in Figure 14, left column), whereas the alpha ERD from the non-BCG corrected data was -1.32 ± 0.56 dB with the peak alpha frequency of 11 Hz (see bottom row in Figure 14, left column). In Figure 15b (left column), the cluster-based permutation test revealed significant differences ($p < .05$) between the beamforming BCG corrected data (visual alpha VE) and corresponding non-BCG corrected electrodes (Oz), indicating that the beamforming technique better recovered the meaningful task-induced activity (visual alpha ERD) which was not present at the sensor level. The significant cluster also revealed the large effect size ($d = 1.06$) (Figure 15b, left column).

By comparing the standard AAS approach (AAS BCG corrected data) and beamforming + AAS BCG corrected data (Figure 15a, left column), the cluster-based permutation test revealed significant differences ($p < .05$) between the beamforming + AAS BCG corrected data (visual alpha VE) and corresponding AAS BCG corrected

electrodes (Oz), suggesting the beamforming spatial filtering could improve the SNR of the meaningful task-induced activity (visual alpha ERD), when compared to the standard AAS approach in the sensor space. Furthermore, the cluster-based permutation test (Figure 15c, left column) revealed significant differences ($p < .05$) between the beamforming BCG corrected data (visual alpha VE) and corresponding AAS BCG corrected electrodes (Oz), demonstrating that the task-induced activity of this beamforming BCG denoising data (Figure 14) had significantly greater SNR when compared to that of the conventional AAS approach (Figure 10). These significant clusters also revealed the small to medium effect sizes ranged from the non-directional $d = 0.14$ to $d = 0.71$ (Figure 15, left column). By comparing the task-induced activity of both beamforming approaches (beamforming + AAS BCG corrected, beamforming BCG corrected), the permutation test revealed no significant difference between them in the visual alpha VE (Figure 11).

Signal-to-noise ratios

The group mean SNR of the visual alpha VE from the beamforming BCG corrected data was 1.03 ± 0.42 (mean $\pm SD$), whereas the group mean SNR of the visual alpha VE from the beamforming + AAS BCG corrected data was 0.99 ± 0.40 (mean $\pm SD$). Both SNRs obtained the source level after beamforming spatial filtering was more than twice as large as the SNRs in the occipital and parietal electrodes ranging

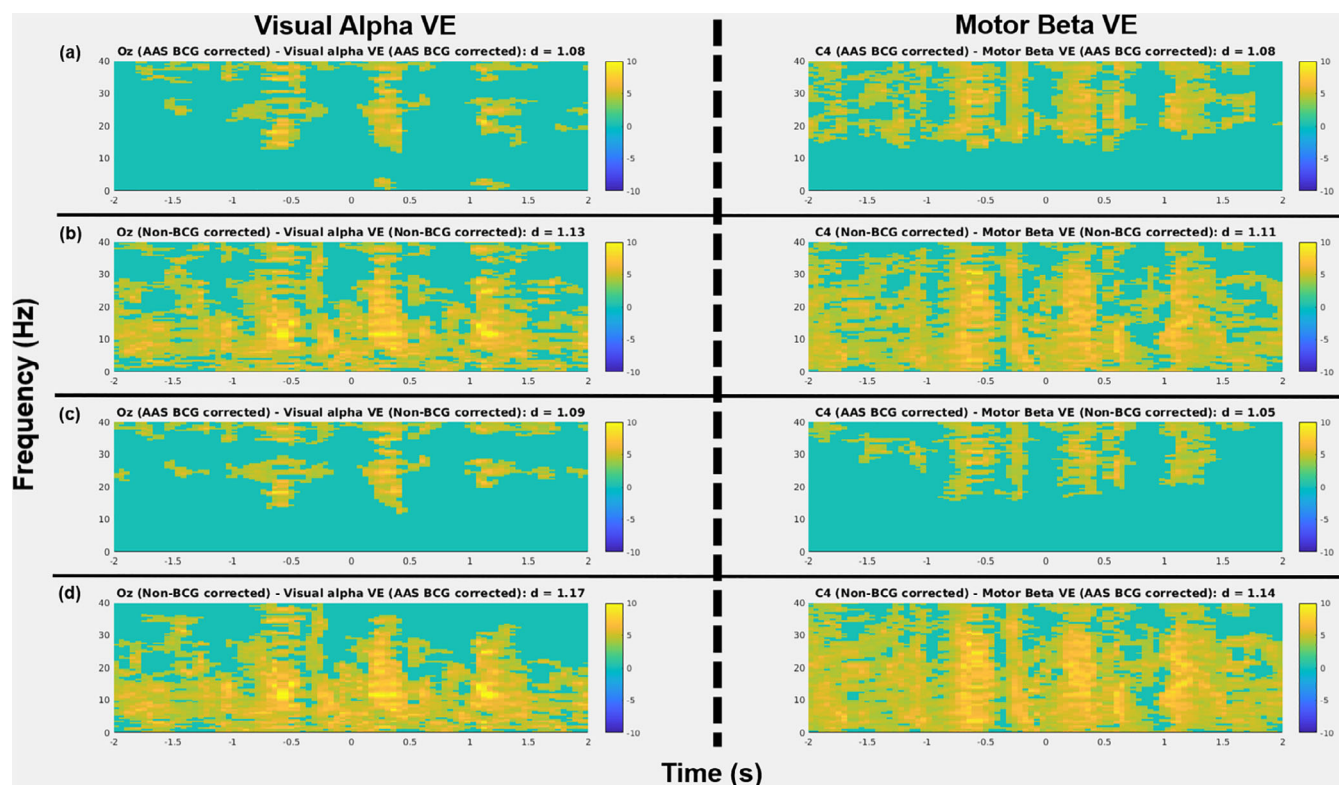


FIGURE 9 R-peak locked analysis: The t-maps of differences between the time–frequency representations (TFRs) for various comparisons, (a) between beamforming + average artefact subtraction (AAS) ballistocardiogram (BCG) corrected and corresponding AAS BCG corrected electroencephalography (EEG) electrodes (Oz for visual, C4 for motor) (“AAS BCG corrected” minus “beamforming + AAS BCG corrected”), (b) between beamforming BCG corrected and corresponding non-BCG corrected EEG electrodes (“non-BCG corrected” minus “beamforming BCG corrected”), (c) between beamforming BCG corrected and corresponding AAS BCG corrected EEG electrodes (“AAS BCG corrected” minus “beamforming BCG corrected”), (d) between beamforming + AAS BCG corrected and corresponding non-BCG corrected EEG electrodes (“non-BCG corrected” minus “beamforming + AAS BCG corrected”), in the visual alpha virtual electrode (VE) in the left column and the motor beta VE in the right column. Figures demonstrate t-values masked by the significant clusters from cluster-based permutation tests ($p < .05$), and if there is a significant cluster, Cohen's d is calculated as the effect size. Yellow denotes a positive t-value showing greater power in the sensor-level data as compared to the source-level data, whereas blue denotes a negative t-value revealing greater power in the source-level data as compared to the sensor-level data

between 0.30 and 0.43 in the sensor level of the BCG corrected signals (see Figure 16), which is consistent with the permutation test results.

3.2.2 | Motor beta ERD

Analysis at the sensor level

Figure 12 shows the group average TFRs measured in the central electrodes (frontal, central, and parietal) for beta (13–30 Hz) power change during the motor preparation/planning before the movement onset for the AAS BCG corrected data (top row) and non-BCG corrected data (bottom row). Although the broadband increases in power (red vertical stripes occurred at the time of 0 s which was the button press for the task responses) revealing the motion artefacts caused by the button press for the task responses can be observed (see Supplementary Figure S5), beta power decrease (beta ERD) was observed within the time window before the movement onset as

compared to baseline time-window (–3 to –2 s prior to the movement onset) in the AAS BCG corrected data (see top row in Figure 12). However, this beta ERD was difficult to identify in the same electrodes from the non-BCG corrected data (see bottom row in Figure 12) as the beta power within the active time-window (–1.25 to –0.25 s before the movement onset) was reduced from -0.92 ± 0.23 dB (AAS BCG corrected data) to -0.78 ± 0.25 dB (non-BCG corrected data) in the C4 electrode and from -1.03 ± 0.21 dB (AAS BCG corrected data) to -0.91 ± 0.30 dB (non-BCG corrected data) in the P4 electrode, revealing that the BCG artefacts, which are typically below 20 Hz, were masking the beta power change related to the movement preparation/planning. In Figure 13, the cluster-based permutation tests demonstrated that significant differences ($p < .05$) between the AAS BCG corrected and non-BCG corrected data were observed in the frontal, central, and parietal electrodes (F4, C4, P4) particularly in the right hemisphere which is contralateral to the left-hand button press, confirming that the motor beta ERD was visible at the contralateral

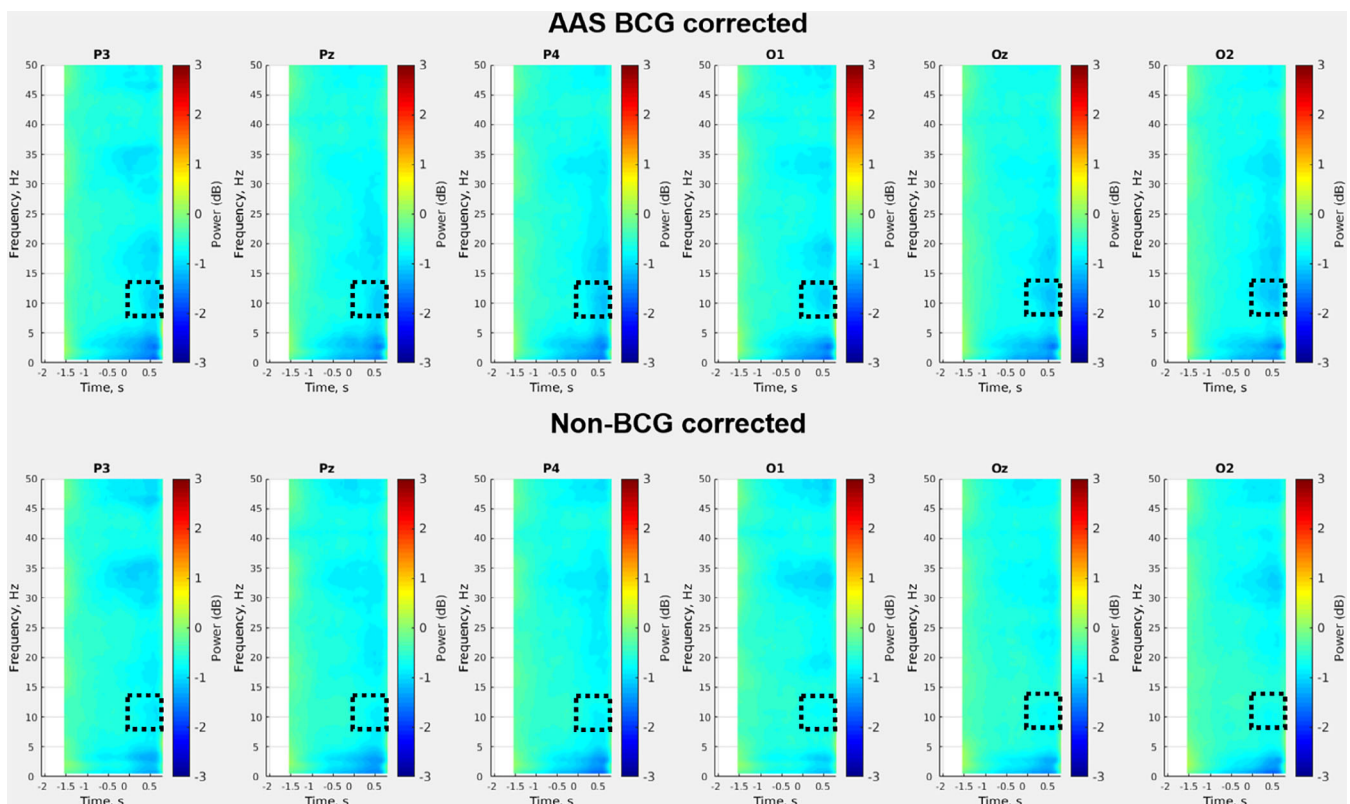


FIGURE 10 Group mean ($N = 20$) time–frequency representations (TFRs) of visual alpha (8–13 Hz) event-related desynchronization (ERD) in response to the target cues which occurred at 600 ms after the probe cue onset (either no cue, double cue, or spatial cue) from six electrodes in the occipital and parietal regions for the average artefact subtraction (AAS) ballistocardiogram (BCG) corrected data (top row) and non-BCG corrected data (bottom row). These TFRs demonstrated -2 to 0.75 s relative to the probe cue onset removing a period of the motion artefacts caused by the button press for the task responses occurring at around 1 s. Open dashed rectangles represent the a priori time (0.1 – 0.75 s) and frequency (alpha: 8 – 13 Hz) of interest for our analysis. The whole trial epoch (-2 to 3 s relative to the probe cue onset) can be seen in Supplementary figure (Figure S4)

frontal, central, and parietal electrodes in the standard AAS BCG corrected data when compared to the non-BCG corrected data at the sensor level. Furthermore, the significant clusters revealed the large to very large effect sizes ranged from $d = 1.08$ to $d = 1.21$ (Figure 13).

Beamforming source reconstructions

Figure 14 (right column) shows the group average TFRs measured in the motor beta VE for beta (13 – 30 Hz) power change during the motor preparation/planning before the movement onset for the AAS BCG corrected data (top row) and non-BCG corrected data (bottom row). Although the broadband increases in power (red vertical stripes occurred at the time of 0 s which was the button press for the task responses) revealed the motion artefacts caused by the button press for the task responses, beta power decrease (beta ERD) was observed within the time window before the movement onset as compared to baseline time-window (-3 to -2 s prior to the movement onset) in both AAS BCG corrected and non-BCG corrected data (right column in Figure 14). The beta ERD within the active time-window (-1.25 to -0.25 s before the movement onset) from the AAS BCG corrected data was -0.95 ± 0.23 dB with the peak beta frequency of 18.5 Hz

(see top row in Figure 14, right column), whereas the beta ERD from the non-BCG corrected data was -1.04 ± 0.21 dB with the peak beta frequency of 18 Hz (see bottom row in Figure 14, right column). In Figure 15b (right column), the cluster-based permutation test revealed significant differences ($p < .05$) between the beamforming BCG corrected data (motor beta VE) and corresponding non-BCG corrected electrodes (C4), indicating that the beamforming technique recovered the meaningful task-induced activity (motor beta ERD) which was not present at the sensor level. The significant clusters also revealed the small effect sizes ($d = -0.28$) (Figure 15b, right column).

By comparing with the standard AAS BCG corrected data, the cluster-based permutation tests revealed significant differences ($p < .05$) between the beamforming + AAS BCG corrected data (motor beta VE) and corresponding AAS BCG corrected electrodes (C4) (Figure 15a, right column), as well as significant differences ($p < .05$) between the beamforming BCG corrected data (motor beta VE) and corresponding AAS BCG corrected electrodes (C4) (Figure 15c, right column), indicating that both beamforming approaches data (Figure 14) increased SNR significantly when compared to that of the conventional AAS approach (Figure 12). These significant clusters also revealed the large to very large effect sizes

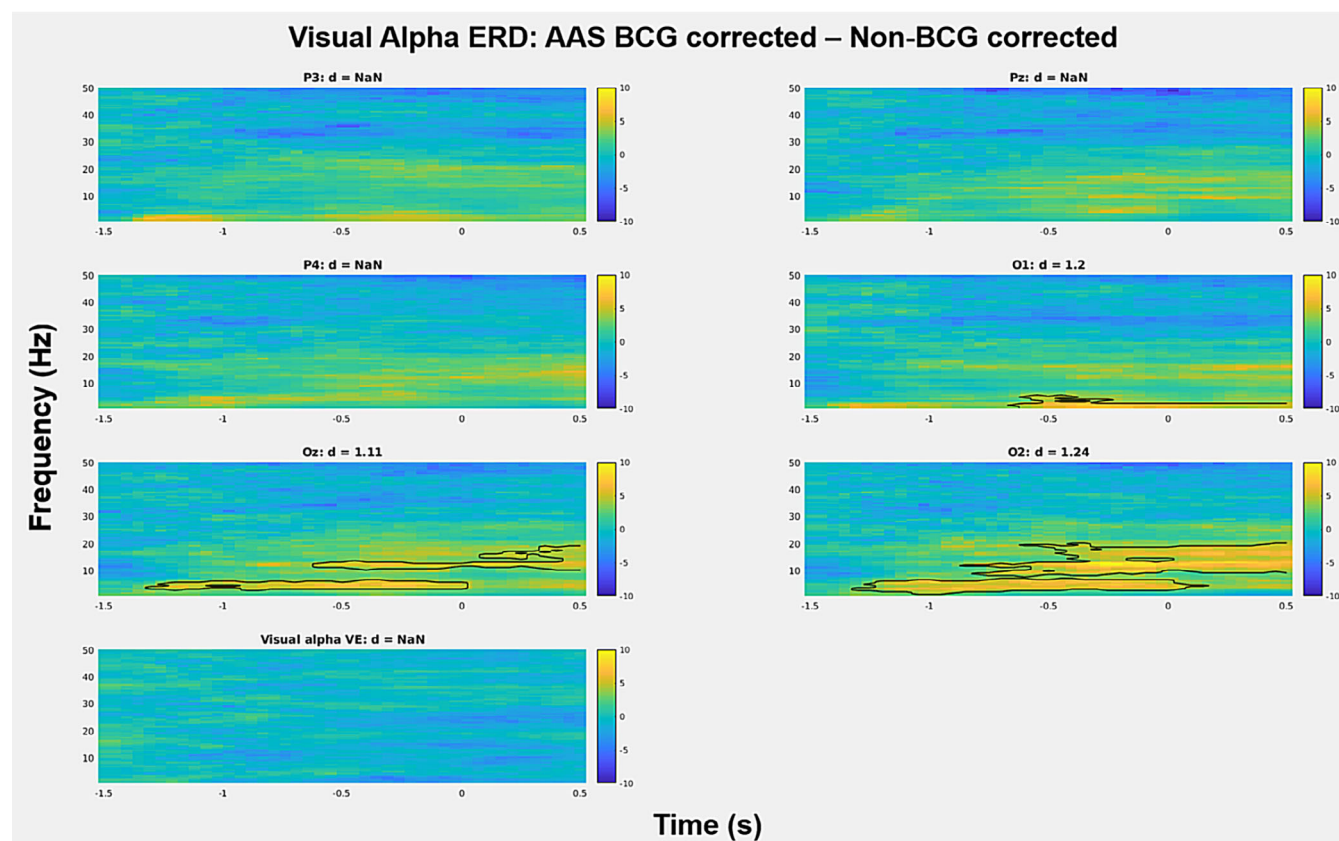


FIGURE 11 Alpha event-related desynchronization (ERD) induced during ANT: The t-maps of differences in the time–frequency representations (TFRs) between the average artefact subtraction (AAS) ballistocardiogram (BCG) corrected and non-BCG corrected data at six electrodes selected from the occipital and parietal regions, and visual alpha virtual electrode (VE). Figures demonstrate t-values and black contour representing the significant clusters from cluster-based permutation tests ($p < .05$), and if there is a significant cluster, Cohen's d is calculated as the effect size. Yellow denotes a positive t-value showing greater power in the AAS BCG corrected data as compared to the non-BCG corrected data, whereas blue denotes a negative t-value revealing greater power in the non-BCG corrected data as compared to the AAS BCG corrected data. The figures suggest that AAS BCG corrected data were able to identify a significantly larger ERD decrease in alpha power, when compared to non-BCG corrected data on the occipital electrodes

ranged from non-directional $d = 0.92$ to $d = 1.49$ (Figure 15, right column). By comparing the task-induced activity of both beamforming approaches (beamforming + AAS BCG corrected, beamforming BCG corrected), the permutation test revealed a significant difference ($p < .05$) between them in the motor beta VE (Figure 13), demonstrating that the beamforming BCG corrected data had significantly larger beta ERD than the beamforming + AAS BCG corrected data. This significant cluster also revealed the large effect size of $d = -1.17$ (Figure 13).

Signal-to-noise ratios

The group average SNR of the motor beta VE from the non-BCG corrected data was 1.31 ± 0.29 (mean \pm SD), whereas the group mean SNR of the motor beta VE from the AAS BCG corrected data was 1.21 ± 0.32 (mean \pm SD). Both SNRs in the source level were more than 1.3 times as large as the SNRs in the sensor level for frontal, central, and parietal electrodes, ranging between 0.68 and 0.88 in the sensor level of the AAS BCG corrected signals (see Figure 16), which is consistent to the permutation test results.

4 | DISCUSSION

In this study, we first investigated the effect of the beamforming technique to attenuate BCG artefacts in EEG–fMRI data, even without detecting cardiac pulse (R-peak) events from simultaneous ECG recordings. In a second step, we also quantified how this technique would preserve expected brain activity induced by the ANT task, while suppressing the BCG artefacts. The beamforming technique is an adaptive spatial filtering technique scanning independently each location in a predefined region of interest (ROI) within the source space, proposed for source localization of EEG and MEG data (Gross et al., 2001; Robinson & Vrba, 1999; Sekihara et al., 2001; van Drongelen et al., 1996; van Veen et al., 1997; van Veen & Buckley, 1988). Moreover, several studies have demonstrated that beamformer is highly efficient when attenuating artefactual signals which have different spatial origins from the underlying signal of interest such as eye movements (Cheyne et al., 2006) and orthodontic metal braces (Cheyne et al., 2007) in MEG. Specifically, the beamforming spatial filter rejects sources of signal variance that are

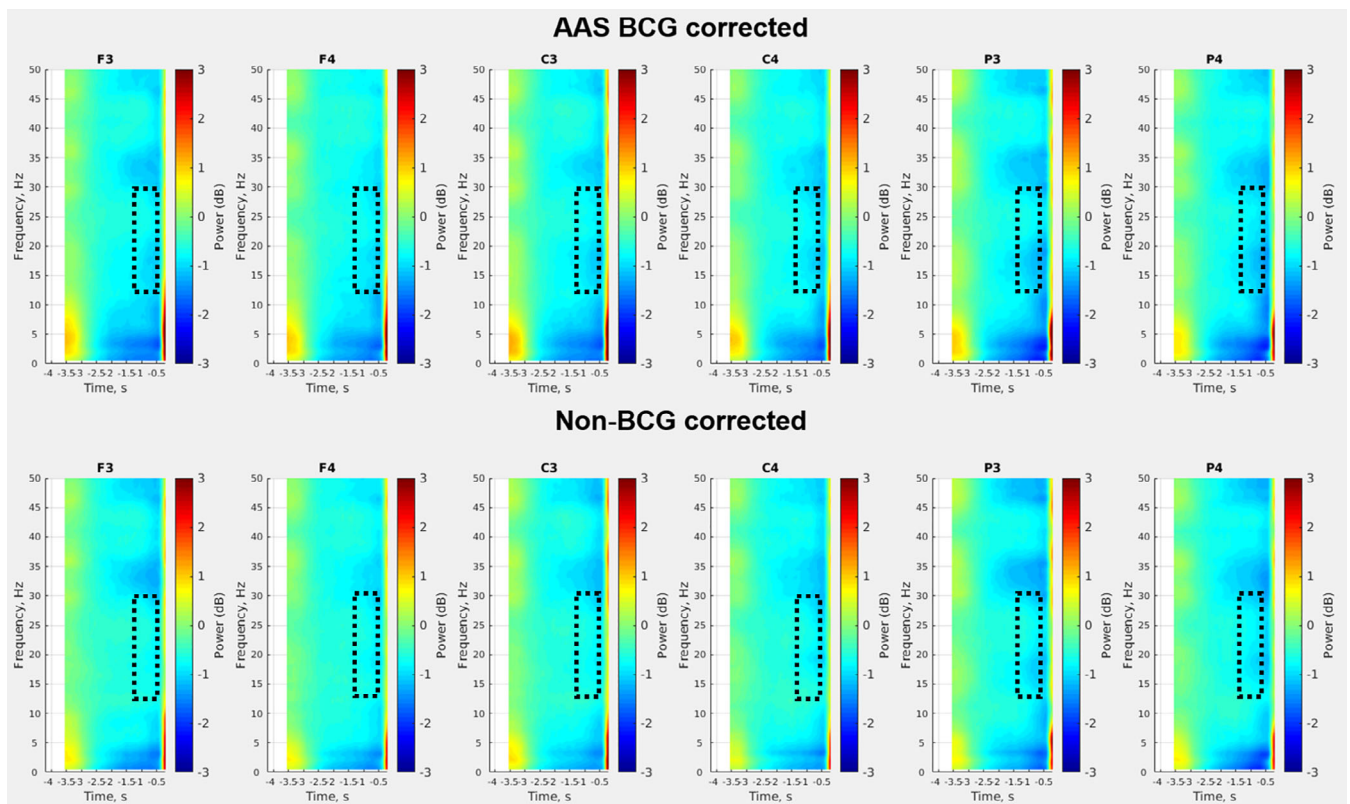


FIGURE 12 Group mean ($N = 20$) time–frequency representations (TFRs) of motor beta (13–30 Hz) event-related desynchronization (ERD) during motor preparation/planning before the movement onset from six electrodes in the frontal, central and parietal regions for the average artefact subtraction (AAS) ballistocardiogram (BCG) corrected data (top row) and non-BCG corrected data (bottom row). These TFRs demonstrated -4 to -0.25 s relative to the movement onset removing a period of the motion artefacts caused by the button press for the task responses occurring at 0 s. Open dashed rectangles represent the a priori time (-1.25 to -0.25 s) and frequency (beta: 13–30 Hz) of interest for our analysis. The whole trial epoch (-4 to 2 s relative to the movement onset) can be seen in Supplementary figure (Figure S5)

not concordant in predetermined source locations in the brain based on the forward model, and attenuates all unwanted source activities outside of the predetermined source location of interest in the data (e.g., eye movements) without having to specify the location or the configuration of these unwanted underlying source signals (Brookes et al., 2007; Huang et al., 2004; van Veen et al., 1997). Since the beamforming spatial filtering appears another promising denoising technique in the context of EEG–fMRI studies (Brookes et al., 2009; Brookes, Mullinger, et al., 2008; Mullinger & Bowtell, 2011), we hypothesized that the beamforming technique would attenuate the BCG artefacts to a similar extent as compared to the conventional AAS BCG artefact corrections.

4.1 | BCG corrections in EEG–fMRI

In the sensor space using time-course (Figures 2 and 3) and time–frequency analysis (Figures 4 and 5), we first showed that generally the standard AAS method demonstrated significant suppression of BCG artefacts by comparing the AAS BCG corrected and non-BCG corrected data, while some of the residual BCG artefacts were still observed above 20 Hz (Figure 6). We then evaluated the impact of

beamforming spatial filtering, when applied to both AAS BCG corrected (beamforming + AAS BCG corrected) and non-BCG corrected (beamforming BCG corrected) data, comparing with sensor level data (AAS BCG corrected data).

The VE locations were determined by the ANT task activity, resulting in one VE in the visual cortex (visual alpha VE) to monitor alpha power decrease induced by visual cues, and one VE in the motor cortex (motor beta VE) to monitor beta power decrease induced by finger tapping preparation/planning. The location of these VEs was estimated specifically for each subject and was found overall concordant at the group level (Figure 7). Based on the two VE locations, we demonstrated that the VE time-courses from both beamforming approaches (beamforming BCG corrected; beamforming AAS + BCG corrected) contained less BCG artefacts when compared to the original uncorrected data in the sensor level (Figure 9b,d). Moreover, both beamforming approaches revealed significantly less BCG artefacts as compared to the standard AAS BCG corrected data (Figure 9a,c). Furthermore, when applying the beamforming to the AAS BCG corrected data, this approach was significantly better than solely applying the beamforming to the uncorrected data (Figures 6 and 8). Overall, our findings demonstrated that the denoising performance of the beamforming BCG corrections was significantly better than the level

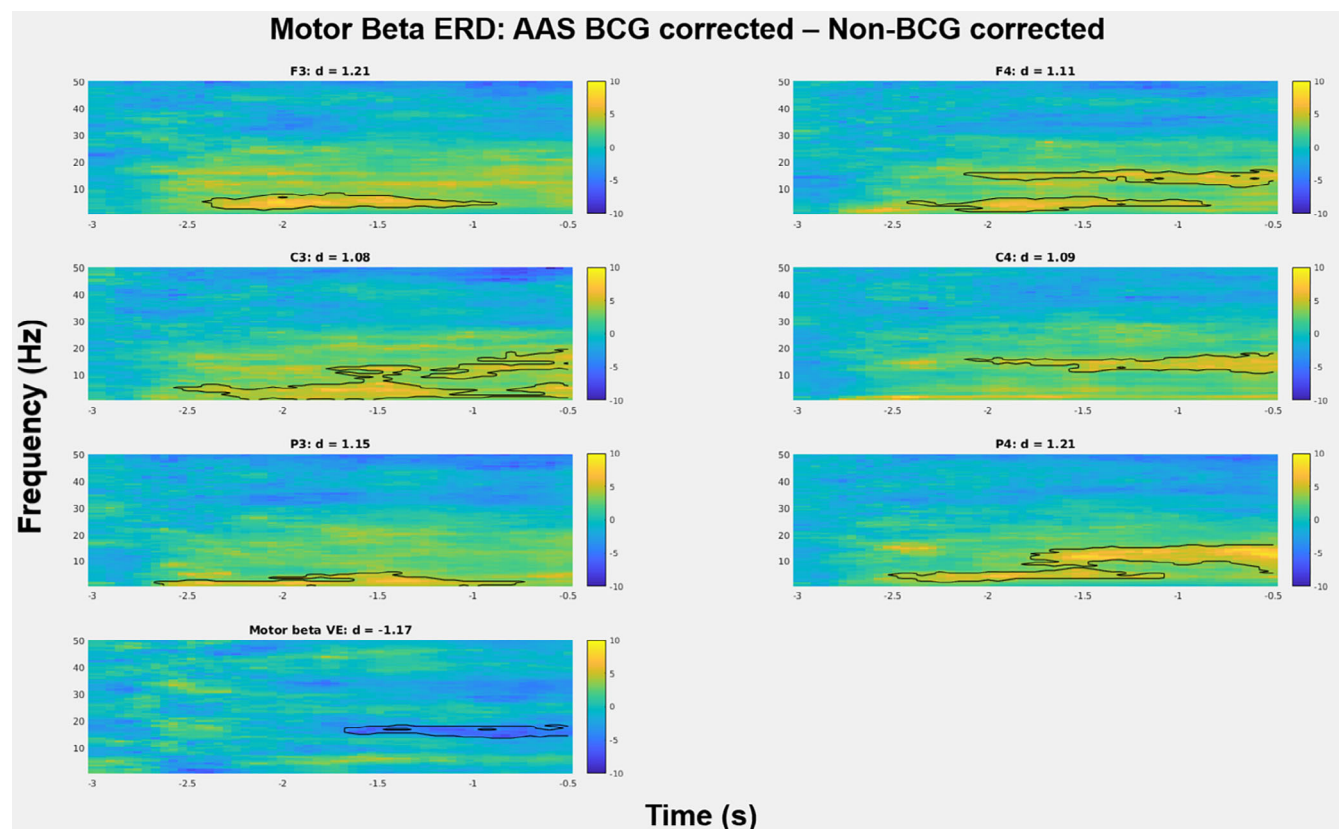


FIGURE 13 Beta event-related desynchronization (ERD) induced during ANT: The t-maps of differences in the time–frequency representations (TFRs) between the average artefact subtraction (AAS) ballistocardiogram (BCG) corrected and non-BCG corrected data at six electrodes selected from the frontal, central and parietal regions, and motor beta virtual electrode (VE). Figures demonstrate t-values and black contour representing the significant clusters from cluster-based permutation tests ($p < .05$), and if there is a significant cluster, Cohen's d is calculated as the effect size. Yellow denotes a positive t-value showing greater power in the AAS BCG corrected data as compared to the non-BCG corrected data, whereas blue denotes a negative t-value revealing greater power in the non-BCG corrected data as compared to the AAS BCG corrected data. The figures suggest that AAS BCG corrected data were able to identify a significantly larger ERD decrease in beta power, when compared to non-BCG corrected data in the frontal, central, and parietal electrodes. Furthermore, beamforming BCG corrected data exhibited larger beta ERD than beamforming + AAS corrected data

of the standard AAS approach. Our results support and extend the previous findings of Brookes, Mullinger, et al. (2008) and Brookes, Vrba, et al. (2008) which had a limited number of participants ($N = 2$) and did not use any statistical analysis. Our findings revealed that this data-driven beamforming denoising approach even without detecting R-peak events from ECG recording is promising when attenuating the BCG artefacts in EEG–fMRI.

Although the AAS BCG correction is commonly used and reported in the EEG–fMRI literature, there are several different approaches to correct the BCG artefacts considering both software (ICA: Debener et al., 2007; OBS: Niazy et al., 2005) and hardware (Reference layer artefact subtraction: Chowdhury et al., 2014; Carbon-wire loop: Masterton et al., 2007; Optical Motion tracking system: LeVan et al., 2013) based solutions. In the software solutions, the ICA technique has been suggested to remove independent components (ICs) corresponding to the BCG artefacts. In the context of the ICA approaches, several different approaches have been suggested, and the selection of the ICs varies based on (a) thresholding the correlation coefficients (i.e., > 0.2) between each

IC and the simultaneously acquired ECG signal (Mantini et al., 2007) or a pulse artefact/BCG template (Srivastava, Crottaz-Herbette, Lau, Glover, & Menon, 2005), (b) applying the autocorrelation function of each IC to find a repeating pattern in EEG (Vanderperren et al., 2010), (c) identifying ICs that exhibit spectral peaks at cardiac-related frequencies (Vanderperren et al., 2007), (d) thresholding averaged peak-to-peak amplitudes of ICs reconstructed signals (i.e., 15 and 25%) when epoched around the cardiac peak (Vanderperren et al., 2010), and (e) identifying ICs explaining the largest amount of variance of the evoked BCG artefacts (Debener et al., 2008). Although the ICA-based approach demonstrated successful BCG suppressions, this method needs more fined parameter tuning. Therefore, in the ICA approaches, the objective and accurate classifications/selections of BCG-related ICs remain a major concern (Abreu et al., 2016; Vanderperren et al., 2010).

The OBS approach is another software solution, which uses principal component analysis (PCA) to remove the principal components (PCs) representing the BCG artefacts. The OBS relies on the assumption that each BCG artefact occurrence in each channel is

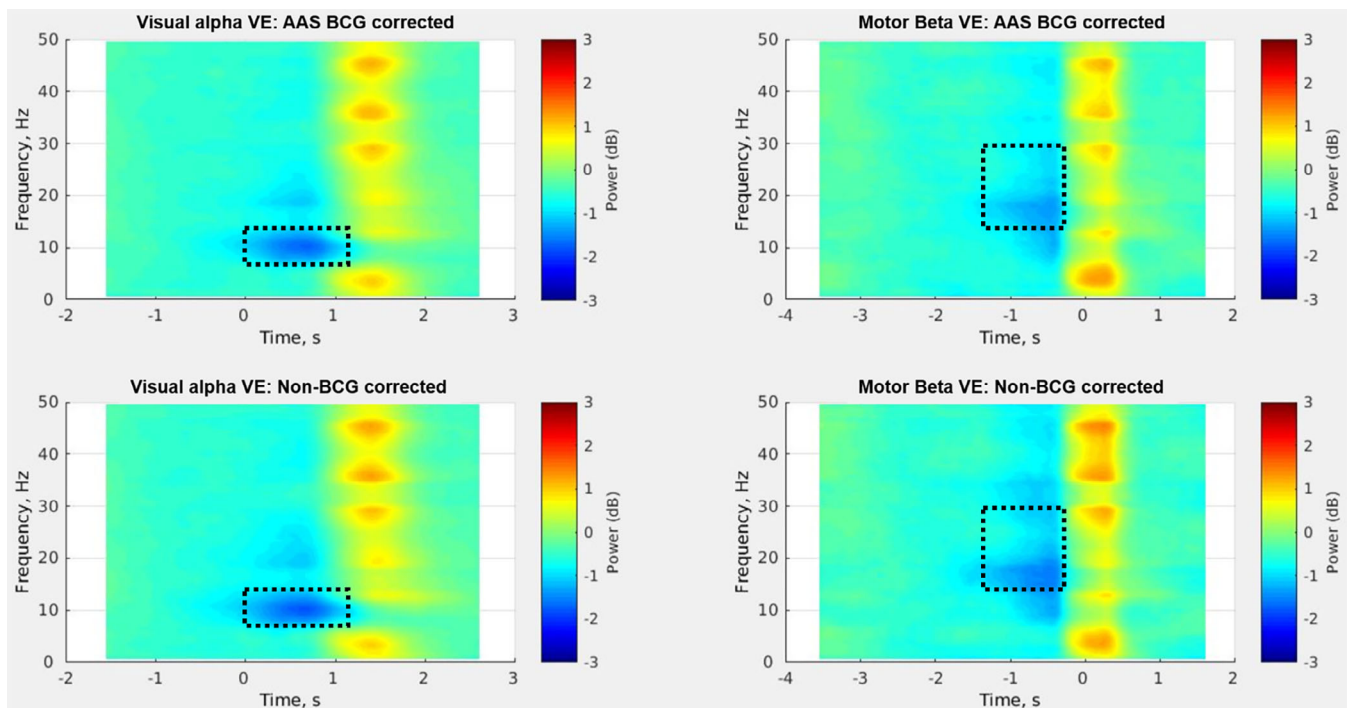


FIGURE 14 Group mean ($N = 20$) time–frequency representations (TFRs) of visual alpha (8–13 Hz) event-related desynchronization (ERD) in response to the target cues which occurred at 600 ms after the probe cue onset (either no cue, double cue, or spatial cue) from the visual alpha virtual electrode (VE) location for the average artefact subtraction (AAS) ballistocardiogram (BCG) corrected data (top row) and non-BCG corrected data (bottom row) in the left column, whereas group mean ($N = 20$) TFRs of motor beta (13–30 Hz) ERD in response to the movement onset from the motor beta VE location for the AAS BCG corrected data (top row) and non-BCG corrected data (bottom row) in the right column. The broadband increases in power (yellow-red vertical stripes) revealed the motion artefacts caused by the button press for the task responses. The open dashed rectangles in the left column represent the a priori time (0.1–1.1 s) and frequency (alpha: 8–13 Hz) of interest for our analysis, whereas the open dashed rectangles in the right column represent the a priori time (–1.25 to –0.25 s) and frequency (beta: 13–30 Hz) of interest for our analysis

independent of any previous occurrence, and OBS of PCs is used for the template creation and subsequent BCG artefact subtractions (Niazy et al., 2005). In comparison to ASS, PCA considered in OBS will allow modelling some variability in the BCG artefact, as opposed to considering the mean effect only. In the OBS approach, one parameter needs to be determined, which is the number of PCs used to create the artefact template. Most studies use the recommended value of 3 or 4 for this parameter (Niazy et al., 2005; Vanderperren et al., 2010), although there is no consensus on whether this number can yield satisfactory corrections for all channels of all datasets (Jorge, Bouloc, Bréchet, Michel, & Gruetter, 2019; Marino et al., 2018; Vanderperren et al., 2010). As different from the ICA approach, the OBS method requires the detections of cardiac peak timing similarly to the AAS approach. Although both ICA and OBS approach have successfully removed the BCG artefacts, using some arbitrary classifications/selections in necessary parameters of both approaches remains a major concern, since both approaches have some risk of aggressively suppressing the meaningful signals too much (Abreu et al., 2016; Vanderperren et al., 2010). Moreover, the common application of the ICA and OBS approach have been proposed after the AAS BCG correction to remove the residual BCG artefacts and successfully improved the AAS BCG correction (Abreu et al., 2018).

Considering these software solutions (ICA and OBS), the AAS approach has still been commonly used and reported in the EEG–fMRI literature. Additionally, this approach has still been recognized as the standard approach (Abreu et al., 2018). However, this AAS approach requires high precisions of the cardiac pulse (R-peak) event detections in the MRI scanner which are used for subtracting averaged BCG artefact templates. Normally R-peak events are detected from simultaneous ECG recordings (see Supplementary Figure S2), although facial and temporal electrodes of high-density EEG can also be used for the detection (Iannotti et al., 2015). ECG signals in the MRI scanner are often distorted (see Supplementary Figure S2), which may prove to be even more problematic when difficulties in obtaining an adequate quality ECG trace occur (i.e., high field MRI, ECG saturation) (Chia et al., 2000; Mullinger, Morgan, & Bowtell, 2008), and significantly time-consuming when additional manual correction is required. Detecting R-peak events from the ECG is thus difficult, so that this procedure may sometimes become unreliable, although VCG instead of ECG recording is more suited and recommended to use for the R-peak detections if available (Mullinger & Bowtell, 2011) because the VCG signals are not distorted as compared to the ECG signals in the MRI. Moreover, there is also inter- and intra-subject variabilities of the latency between the ECG and BCG events (Iannotti

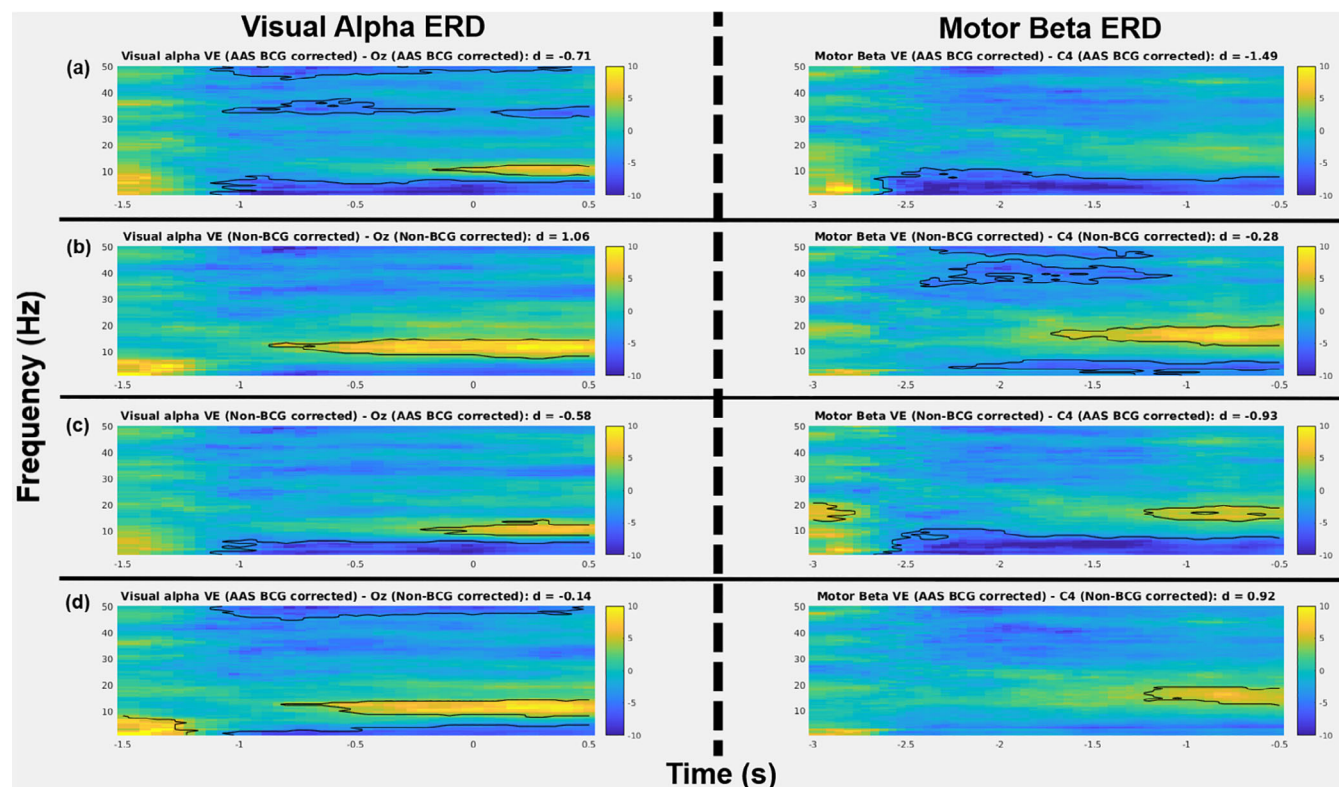


FIGURE 15 Alpha and beta event-related desynchronization (ERD) induced during ANT: The t-maps of differences between the time-frequency representations (TFRs) for various comparisons, (a) between beamforming + average artefact subtraction (AAS) ballistocardiogram (BCG) corrected and corresponding AAS BCG corrected electroencephalography (EEG) electrodes, (b) between beamforming BCG corrected and corresponding non-BCG corrected EEG electrodes, (c) between beamforming BCG corrected and corresponding AAS BCG corrected EEG electrodes, (d) between beamforming + AAS BCG corrected and corresponding non-BCG corrected EEG electrodes, in the visual alpha ERD in the left column and the motor beta ERD in the right column. Figures demonstrate t-values and black contour representing the significant clusters from cluster-based permutation tests ($p < .05$), and if there is a significant cluster, Cohen's d is calculated as the effect size. Yellow denotes a positive t-value showing greater power in the source-level data as compared to the sensor-level data, whereas blue denotes a negative t-value revealing greater power in the sensor-level data as compared to the source-level data

et al., 2015), which will have negative impact on the AAS performance. Despite known limitations of the AAS approach, the AAS approach has been used as some ground truth in EEG-fMRI to demonstrate the denoising performance of new techniques. Considering the difficulty and imprecise R peak detections, our proposed data-driven beamforming denoising technique is promising, demonstrating the advantages of neither relying on ECG signals nor needing to determine some parameters as compared to the other correction techniques (ICA, OBS). In this study, solely applying the beamforming spatial filtering technique to the uncorrected data demonstrated superior denoising performance than the standard AAS BCG correction. This data-driven beamforming technique could be well suited for longer EEG-fMRI data acquisition, such as sleep or resting-state data or epilepsy monitoring, where varieties of cardiac responses would be expected to be large and the risk of losing or saturating ECG signals would be high. Under these conditions, the AAS and other software solutions might not be efficient. Based on our findings, this data-driven approach could be applied to suppress the BCG artifacts without having to use the detected R-peak events from ECG recordings during the long acquisition.

4.2 | Task-based-induced neural activity in EEG-fMRI

Having successfully demonstrated the effect of the beamforming technique to suppress the BCG artifacts, it was crucial to also demonstrate that this technique would not significantly suppress meaningful EEG signals, but rather preserve them. In this study, we investigated whether this beamforming technique could recover the meaningful task-based-induced neural activities indicated by visual alpha (8–13 Hz) ERD during observing visual stimuli and motor beta (13–30 Hz) ERD during movement preparation/planning before the movement onset during ANT (Fan et al., 2005, 2007). First, we demonstrated that the standard AAS BCG corrected data indeed exhibited greater alpha ERD during the visual stimuli in the occipital electrodes (Figures 10 and 11), and greater beta ERD during the movement preparation in the central electrodes contralateral to the left hand button press as compared to the non-BCG corrected data (Figures 12 and 13). Applying the beamforming technique to both AAS BCG corrected and non-BCG corrected data, we then demonstrated that both beamforming approaches (beamforming + AAS BCG corrected,

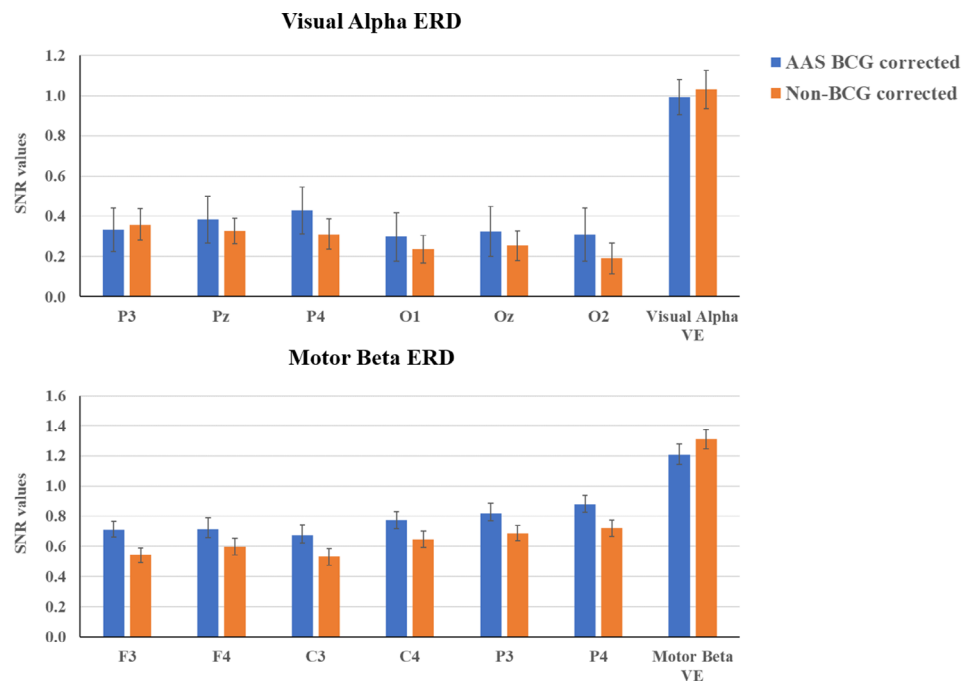


FIGURE 16 Group mean ($N = 20$) signal-to-noise ratios (SNRs) (\pm SD) of visual alpha (8–13 Hz) event-related desynchronization (ERD) for the six electrodes of occipital and parietal regions and visual alpha virtual electrode (VE) location from both average artefact subtraction (AAS) BCG corrected and non-BCG corrected data in the top row, and group mean ($N = 20$) SNRs (\pm SE) of motor beta (13–30 Hz) ERD for the six electrodes of frontal, central, and parietal regions and motor beta VE location from both AAS BCG corrected and non-BCG corrected data in the bottom row. SNRs were calculated by dividing mean signal in the frequency of interest within the active time window by the SD of signals in the frequency of interest within the baseline time window, then group mean SNR was calculated averaging averaged individual subject's SNRs across trials (in a similar approach to Hill et al. (2020))

beamforming BCG corrected) exhibited greater alpha ERD with the peak alpha frequency of 11 Hz during the visual stimuli in the visual alpha VE, and greater beta ERD with the peak beta frequency of around 18 Hz during the movement preparation in the motor beta VE as compared to the non-BCG corrected data (Figures 14 and 15b,d). Furthermore, as compared to the AAS BCG corrected data, both beamforming approaches demonstrated clearer alpha ERD and beta ERD by suppressing any residual artefacts caused by fMRI acquisition (Figure 15a,c). Considering the effect of the data-driven beamforming approaches, the beamforming BCG corrected data revealed significantly greater motor beta ERD as compared to the beamforming + AAS BCG corrected data (Figure 13), whereas there was no significant difference in the visual alpha ERD (Figure 11). Additionally, the locations of visual alpha VEs in the visual cortex were consistent with the previous findings when the visual stimuli were used to trigger movement executions (Brookes et al., 2005; Scheeringa et al., 2011; Wilson et al., 2019), whereas the locations of motor beta VEs were found as expected in the right motor cortex contralateral to the left-hand button presses (Hill et al., 2020; Wilson et al., 2019). Based on these robust visual alpha ERD and motor beta ERD and VE locations, our findings revealed that our data-driven beamforming approach did not only suppress the BCG artefacts, but also recovered meaningful task-based neural signals induced by the ANT task (Fan et al., 2007; Marshall et al., 2015).

4.3 | SNRs between sensor and source space

Findings of the visual alpha and motor beta ERDs together demonstrated both beamforming approaches (beamforming + AAS BCG corrected and beamforming BCG corrected data) successfully recovered the expected task-based-induced neural activity during visual stimuli or preparation/planning of the movement execution respectively, while minimizing the effects of the BCG artefacts. Furthermore, SNR analysis revealed that the group mean SNRs of the visual alpha VEs from both beamforming approaches in the source level increased the SNRs by more than twice when compared to the SNR measured at the sensor level (Figure 16, top row). The group mean SNRs of the motor beta VEs from both beamforming approaches in the source level increased the SNRs by more than 1.3 times as compared to those in the sensor level, which are consistent with the permutation test results in the TFRs (Figure 16, bottom row).

Indeed, in a recent MEG study, Hill et al. (2020) reported similar beamforming source reconstruction approach improving the SNRs by over 1.5 times for the motor beta frequency activity during finger abduction movements and by over 1.5 times for the visual gamma (55–70 Hz) frequency activity during the visual stimuli when compared to those in the sensor space. As expected, our SNR findings were also consistent with the previous findings suggesting that beamforming source reconstruction will improve the SNRs when

compared to the sensor level (Brookes et al., 2009; Hill et al., 2020; Sekihara et al., 2004), and this approach will be beneficial especially in the EEG-fMRI (Brookes et al., 2009; Mullinger & Bowtell, 2011), which is indeed the advantage of using the beamforming technique in EEG-fMRI.

Another advantage of applying the beamforming technique in EEG-fMRI is to improve the sensitivity and specificity of fMRI BOLD general linear model (GLM) analysis, although the EEG-fMRI data fusion analysis was beyond the aim of this study. This can be achieved by extracting source activities from a selected VE location, calculating the Hilbert transformed envelope of source neural activities in a specific frequency band, and parameterizing regressors with the Hilbert envelope amplitude fluctuations instead of using consistent fixed binary boxcar (i.e., 0 or 1) for the fMRI GLM analysis (Brookes, Mullinger, et al., 2008; Mullinger et al., 2014). This is based on the findings demonstrating that the amplitudes and variabilities of BOLD responses have been better explained by this parameterized GLM (single-trial/event correlation analysis) which takes account of source neural variability in EEG responses than by a conventional GLM of consistent amplitude responses (Grouiller et al., 2011; Mullinger et al., 2014). This Hilbert transformed envelope has been used in the different frequency bands (alpha 8–13 Hz: Mullinger et al., 2013, 2014; Mullinger, Cherukara, Buxton, Francis, & Mayhew, 2017; beta 13–30 Hz: Pakenham et al., 2020; Wilson et al., 2019; and gamma 55–80 Hz: Uji et al., 2018). For example, this parameterized GLM analysis successfully improved the specificity and sensitivity to identify the neurophysiological origin of the negative BOLD response to unilateral median nerve stimulation (Mullinger et al., 2014) and negative BOLD responses between stimulated and unstimulated sensory cortex (Wilson et al., 2019). Furthermore, this GLM analysis revealed that a significant positive correlation between single trial gamma band variability and BOLD responses over the contralateral primary motor cortex during finger abduction movements, indicating that tight coupling of neurovascular coupling between the gamma band activity and BOLD responses (Uji et al., 2018). We assume that such fMRI GLM approach can be used to better localize the neurovascular coupling of sleep specific neural activities (i.e., slow-wave, spindle) in sleep research, after the data-driven beamforming denoising technique suppresses the BCG artefacts which remain problematic for the frequency of sleep specific neural activities.

4.4 | Limitations of beamforming techniques

In this article, we demonstrated that this data-driven beamforming approach did not only significantly attenuate the BCG artefacts without having to use the detected R-peak events from ECG recordings, but also significantly recovered the expected task-based-induced brain activity indicated by alpha and beta ERDs when compared to the conventional AAS BCG corrections. However, this beamforming approach also has some limitations. For the construction of the beamforming spatial filters, realistic head volume conductor modelling is required for accurately computing the EEG and MEG lead-fields

(Brookes, Mullinger, et al., 2008; Neugebauer, Möddel, Rampp, Burger, & Wolters, 2017). The limitation of the beamforming technique comes from the difficulty in accurately calculating the EEG forward solution. More accurate head models based on realistic head geometry obtained from anatomical MR images and knowledge of the accurate location of the EEG electrodes on the head can provide a more accurate forward solution. Whereas access to such information is not always straightforward, in this article, we did consider a realistic head model, consisting of a four-layer (scalp, skull, CSF, and brain) BEM head model from individual anatomical images, with digitized EEG electrode locations using the EGI GPS to facilitate individualized accurate co-registration of electrode positions with each subject's anatomical image.

Another limitation is that better suppressions of MRI-related artefacts require the use of high-density EEG electrodes (at least 64 EEG channels). Brookes et al. (2009) demonstrated that using high-density EEG electrodes improved the level of artefact attenuations increasing SNRs by a factor of around 1.6 if the number of EEG electrodes was increased from 32 to 64 channels when the data was acquired at 7 T MRI. Another major limitation of beamforming technique is that this approach cannot properly reconstruct two spatially separate but temporally correlated sources (Brookes et al., 2007; Huang et al., 2004; Quraan & Cheyne, 2010; van Veen et al., 1997). For example, beamforming cancels each other when spatially far from each other (i.e., auditory steady-state response) (Brookes et al., 2007) or merge when they are spatially placed close to each other (Huang et al., 2004), although a modified source model instead of a standard single source model allows for beamforming reconstruction of the spatially separate but temporally correlated sources (Brookes et al., 2007).

Another important limitation is the selection of an accurate VE location in beamforming source space. Future research first needs to investigate what extent selecting an inaccurate VE location would influence the performance of beamforming approach. In most EEG-fMRI studies, the timing of the EEG events/features is considered more important than its localization, when associated with an fMRI GLM analysis (e.g., detection of epileptic discharges, sleep specific discharges). A commonly used approach for the beamforming technique to select the VE location is to identify a maximum/minimum T score value location in the ROI for any task-based data. Although this approach to select VEs has been used for resting-state data (Hillebrand et al., 2016; Hillebrand, Barnes, Bosboom, Berendse, & Stam, 2012), this way might not be optimal in the sleep research due to the propagation of signals of interest and lack of a clear baseline. This issue could be solved statistically using bootstrapping techniques and permutation tests of source images. The validation of these approaches first needs to be fully investigated and addressed to improve beamforming approaches. Furthermore, since the beamforming technique has been initially introduced for the source imaging technique in MEG and EEG studies (Gross et al., 2001; Robinson & Vrba, 1999; Sekihara et al., 2001; van Drongelen et al., 1996; van Veen et al., 1997; van Veen & Buckley, 1988), future study needs to investigate the source localization performance (VE selections) of

the beamforming approach comparing with any other source imaging technique in the context of EEG–fMRI.

In our findings, there were variances in the VE locations (38 mm in the visual cortex; 14 mm in the motor cortex) between the beamforming + AAS BCG corrected and beamforming BCG corrected data. Therefore, using the same VE locations from the beamforming + AAS BCG corrected data ($[-25 \pm 4, -75 \pm 1, -8 \pm 3]$ mm [MNI:x,y,z] for the visual alpha VE; $[45 \pm 5, -44 \pm 3, 54 \pm 2]$ mm [MNI:x,y,z] for the motor beta VE), the same data analysis was conducted to investigate how much the selection of VEs would influence the beamforming performance. This analysis revealed that a similar level of the beamforming BCG denoising performance was observed (see Supplementary Figures S6 and S7), although the effect of visual alpha ERD and motor beta ERD for the beamforming BCG corrected data during the ANT was reduced (see Supplementary Figures S8 and S9) due to the suboptimal selection of the VEs for the beamforming BCG corrected data. Although our results can at least demonstrate the consistent and similar performance of the beamforming technique on the BCG correction when similar VE regions (i.e., within the range of 38 mm in the visual cortex and 14 mm in the motor cortex) are selected, imprecise detections of the R-peaks might have caused distorted EEG sensor-level signals and therefore influenced the beamforming spatial filtering performance. Consequently, VE selections resulted in the different VE locations between the beamforming + AAS BCG corrected and beamforming BCG corrected data (Figure 7). In general, if a clear and clean ECG trace is acquired and precise R-peak detection is obtained, denoising and cleaning EEG data before applying the beamforming technique should be recommended as observed from the smaller amplitude at the time of R peaks in the time-course signals (see Figure 8) and smaller power fluctuations (see Figures 6 and 8) from the R-peak analysis when compared to the beamforming BCG corrected data. The problem remains to be how to achieve precise R-peak detections, as the ECG signals are distorted in the MRI scanner (see Supplementary Figure S2). Considering these issues, the data-driven beamforming approach would be a promising alternative to correct the BCG artefacts without relying on ECG signals. However, using a simpler and better control study design (i.e., visual checkerboard stimulation, medium nerve stimulation, finger tapping), future research needs to investigate how much benefit can be achieved by further cleaning and denoising the EEG data (e.g., using ICA or OBS) before applying the beamforming technique.

The ANT was chosen as a more suitable task consisting of expected clear baseline periods and clear event onsets in order to investigate the performance of the beamforming technique in EEG–fMRI when compared to the Mackworth Clock Task (Lichstein et al., 2000; Loh et al., 2004) and N-back task (Kirchner, 1958; Sweet, 2011) in this dataset studying the impact of sleep deprivation (Cross et al., 2021). However, the current ANT task design with a fixed duration from the probe cue to the target cue might not be optimal to have a true baseline period, which might have reduced some robust effects of the visual alpha and motor beta ERD, when compared to a simple visual or motor task (*visual alpha ERD*: Brookes et al., 2005; Scheeringa et al., 2011; Wilson et al., 2019; *Motor beta ERD*: Cheyne & Ferrari, 2013; Darvas

et al., 2010; Hall et al., 2011; Muthukumaraswamy, 2010; Pfurtscheller et al., 1996; Pfurtscheller & Lopes da Silva, 1999; Takemi et al., 2013; Uji et al., 2018). Despite this potential limitation, our results still demonstrated the benefit of the beamforming BCG correction during a more challenging cognitive task.

4.5 | Implications

Our beamforming BCG artefact correction approach is a data-driven method neither requiring identifying noise and signal components nor relying on the simultaneous ECG recording, which makes it promising especially for long data acquisition of sleep or resting-state EEG–fMRI. However, pseudo-T statistic maps between the active and passive contrast to identify VE locations might not be feasible and reliable in other contexts like resting state, sleep, or epilepsy studies. Instead, using an anatomical atlas would be an interesting option for the beamforming approach as it has been used in EEG (van Klink et al., 2018) and MEG (Hillebrand et al., 2016, 2012; Youssofzadeh, Agler, Tenney, & Kadis, 2018; Youssofzadeh, Williamson, & Kadis, 2017) beamforming resting-state functional connectivity. Future studies need to investigate this atlas-based beamforming approach in the context of EEG–fMRI. Furthermore, from the current data analysis, this beamforming approach is not intended to replace the standard MRI-related artefact corrections (i.e., AAS, ICA, OBS) when a precise detection of R-peaks is achieved. Our findings also demonstrated the beamforming + AAS BCG corrected data contained significantly less remaining BCG artefacts as compared to the beamforming BCG corrected data. Therefore, beamforming and accurate AAS approach should be considered as complementary and the combination of both should provide better correction than each of them separately.

5 | CONCLUSIONS

In this article, we demonstrated that our data-driven beamforming approach did not only attenuate the BCG artefacts without having to use the detected R-peak events from ECG recordings, but also recovered the expected task-based-induced brain activity indicated by alpha and beta ERDs, which the BCG artefacts typically obscure, in a significantly greater extent than the conventional AAS BCG corrections. Our findings bring new insight into an active area of research in EEG–fMRI-related to the extraction of meaningful brain signals and suppression of MRI-related artefacts. This approach would be very promising and beneficial especially for the sleep EEG–fMRI data without detecting R-peak events from ECG recording. Future research will compare this beamforming BCG artefact correction approach with MRI-related artefact corrections using VCG recordings, and further examine whether this beamforming approach would be better suited to recover meaningful EEG signals related to spontaneous events such as brain rhythms during sleep and epileptic discharges.

ACKNOWLEDGMENTS

This research was supported by the Natural Sciences and Engineering Research Council of Canada (T. T. D.-V.) and the Canada Foundation for Innovation (T. T. D.-V.). The MRI compatible high-density EEG device (Magstim-EGI) and data acquisition were made possible through an internal grant from PERFORM centre and the Faculty of Arts and Science of Concordia University (C. G.). T. T. D.-V. is also supported by the Canadian Institutes of Health Research (MOP 142191, PJT 153115, PJT 156125, and PJT 166167), the Fonds de Recherche du Québec—Santé and Concordia University. C. G. is supported by Natural Sciences and Engineering Research Council of Canada Discovery grants as well as the Canadian Institutes of Health Research (PJT-159948 and MOP-133619) and the Fonds de Recherche du Québec, Nature et Technologie (research team grant). M. U. is supported by a Horizon Postdoctoral Fellowship from Concordia University. U. A. was supported by postdoctoral fellowships from Savoy Foundation and the Fonds de Recherche du Québec—Santé (FRQS).

AUTHOR CONTRIBUTIONS

Makoto Uji: Conceptualization, methodology, formal data analysis, investigation, data curation, writing - original draft, visualization, project administration. **Nathan Cross:** Data acquisition, writing - review and editing. **Florence B. Pomares:** Data acquisition, writing - review and editing. **Aurore A. Perrault:** Data acquisition, writing - review and editing. **Aude Jegou:** Data acquisition, writing - review and editing. **Alex Nguyen:** Data acquisition, writing - review and editing. **Umit Aydin:** Data acquisition, writing - review and editing. **Jean-Marc Lina:** Methodology, validation, writing - review and editing. **Thien Thanh Dang-Vu:** Conceptualization, resources, writing - review and editing, supervision, project administration, funding acquisition. **Christophe Grova:** Conceptualization, resources, writing - review and editing, supervision, project administration, funding acquisition.

DATA AVAILABILITY STATEMENT

All data used in this study will be available via a request to the corresponding author (M. U.). Open access software used in this study is available at <https://sccn.ucsd.edu/eeglab> (EEGLAB) and <http://www.ru.nl/neuroimaging/fieldtrip> (FieldTrip). Custom analysis code used in this study will be available via a request to the corresponding author (M. U.).

ORCID

Makoto Uji  <https://orcid.org/0000-0002-9445-6353>
Nathan Cross  <https://orcid.org/0000-0002-7325-7646>
Florence B. Pomares  <https://orcid.org/0000-0002-1139-9825>
Aurore A. Perrault  <https://orcid.org/0000-0003-2839-610X>
Aude Jegou  <https://orcid.org/0000-0002-4253-4284>
Alex Nguyen  <https://orcid.org/0000-0001-9773-3515>
Umit Aydin  <https://orcid.org/0000-0002-6327-7811>
Thien Thanh Dang-Vu  <https://orcid.org/0000-0002-7235-2721>
Christophe Grova  <https://orcid.org/0000-0003-2775-9968>

REFERENCES

- Abreu, R., Leal, A., & Figueiredo, P. (2018). EEG-informed fMRI: A review of data analysis methods. *Frontiers in Human Neuroscience*, 12, 1–23. <https://doi.org/10.3389/fnhum.2018.00029>
- Abreu, R., Leite, M., Jorge, J., Grouiller, F., van der Zwaag, W., Leal, A., & Figueiredo, P. (2016). Ballistocardiogram artifact correction taking into account physiological signal preservation in simultaneous EEG-fMRI. *NeuroImage*, 135, 45–63. <https://doi.org/10.1016/j.neuroimage.2016.03.034>
- Allen, P. J., Josephs, O., & Turner, R. (2000). A method for removing imaging artifact from continuous EEG recorded during functional MRI. *NeuroImage*, 12, 230–239. <https://doi.org/10.1006/nimg.2000.0599>
- Allen, P. J., Polizzi, G., Krakow, K., Fish, D. R., & Lemieux, L. (1998). Identification of EEG events in the MR scanner: The problem of pulse artifact and a method for its subtraction. *NeuroImage*, 8, 229–239. <https://doi.org/10.1006/nimg.1998.0361>
- Bagshaw, A. P., Aghakhani, Y., Bénar, C. G., Kobayashi, E., Hawco, C., Dubeau, F., ... Gotman, J. (2004). EEG-fMRI of focal epileptic spikes: Analysis with multiple haemodynamic functions and comparison with gadolinium-enhanced MR angiograms. *Human Brain Mapping*, 22, 179–192. <https://doi.org/10.1002/hbm.20024>
- Becker, R., Reinacher, M., Freyer, F., Villringer, A., & Ritter, P. (2011). How ongoing neuronal oscillations account for evoked fMRI variability. *The Journal of Neuroscience*, 31, 11016–11027. <https://doi.org/10.1523/jneurosci.0210-11.2011>
- Bénar, C. G., Schön, D., Grimault, S., Nazarian, B., Burle, B., Roth, M., ... Anton, J. L. (2007). Single-trial analysis of oddball event-related potentials in simultaneous EEG-fMRI. *Human Brain Mapping*, 28, 602–613. <https://doi.org/10.1002/hbm.20289>
- Bonmassar, G., Purdon, P. L., Jääskeläinen, I. P., Chiappa, K., Solo, V., Brown, E. N., & Belliveau, J. W. (2002). Motion and ballistocardiogram artifact removal for interleaved recording of EEG and EPs during MRI. *NeuroImage*, 16(4), 1127–1141. <https://doi.org/10.1006/nimg.2002.1125>
- Brookes, M. J., Gibson, A. M., Hall, S. D., Furlong, P. L., Barnes, G. R., Hillebrand, A., ... Morris, P. G. (2005). GLM-beamformer method demonstrates stationary field, alpha ERD and gamma ERS co-localisation with fMRI BOLD response in visual cortex. *NeuroImage*, 26, 302–308. <https://doi.org/10.1016/j.neuroimage.2005.01.050>
- Brookes, M. J., Mullinger, K. J., Stevenson, C. M., Morris, P. G., & Bowtell, R. (2008). Simultaneous EEG source localisation and artifact rejection during concurrent fMRI by means of spatial filtering. *NeuroImage*, 40, 1090–1104. <https://doi.org/10.1016/j.neuroimage.2007.12.030>
- Brookes, M. J., Stevenson, C. M., Barnes, G. R., Hillebrand, A., Simpson, M. I. G., Francis, S. T., & Morris, P. G. (2007). Beamformer reconstruction of correlated sources using a modified source model. *NeuroImage*, 34, 1454–1465. <https://doi.org/10.1016/j.neuroimage.2006.11.012>
- Brookes, M. J., Vrba, J., Mullinger, K. J., Geirsdóttir, G. B., Yan, W. X., Stevenson, C. M., ... Morris, P. G. (2009). Source localisation in concurrent EEG/fMRI: Applications at 7T. *NeuroImage*, 45, 440–452. <https://doi.org/10.1016/j.neuroimage.2008.10.047>
- Brookes, M. J., Vrba, J., Robinson, S. E., Stevenson, C. M., Peters, A. M., Barnes, G. R., ... Morris, P. G. (2008). Optimising experimental design for MEG beamformer imaging. *NeuroImage*, 39, 1788–1802. <https://doi.org/10.1016/j.neuroimage.2007.09.050>
- Buzsáki, G., Anastassiou, C. A., & Koch, C. (2012). The origin of extracellular fields and currents—EEG, ECoG, LFP and spikes. *Nature Reviews. Neuroscience*, 13, 407–420. <https://doi.org/10.1038/nrn3241>
- Cheyne, D., Bakhtazad, L., & Gaetz, W. (2006). Spatiotemporal mapping of cortical activity accompanying voluntary movements using an event-related beamforming approach. *Human Brain Mapping*, 27, 213–229. <https://doi.org/10.1002/hbm.20178>

- Cheyne, D., Bostan, A. C., Gaetz, W., & Pang, E. W. (2007). Event-related beamforming: A robust method for presurgical functional mapping using MEG. *Clinical Neurophysiology*, 118, 1691–1704. <https://doi.org/10.1016/j.clinph.2007.05.064>
- Cheyne, D., & Ferrari, P. (2013). MEG studies of motor cortex gamma oscillations: Evidence for a gamma “fingerprint” in the brain? *Frontiers in Human Neuroscience*, 7, 1–7. <https://doi.org/10.3389/fnhum.2013.00575>
- Chia, J. M., Fischer, S. E., Wickline, S. A., & Lorenz, C. H. (2000). Performance of QRS detection for cardiac magnetic resonance imaging with a novel vector cardiographic triggering method. *Journal of Magnetic Resonance Imaging*, 12, 678–688. [https://doi.org/10.1002/1522-2586\(200011\)12:5<678::AID-JMRI4>3.0.CO;2-5](https://doi.org/10.1002/1522-2586(200011)12:5<678::AID-JMRI4>3.0.CO;2-5)
- Chowdhury, M. E. H., Mullinger, K. J., Glover, P., & Bowtell, R. (2014). Reference layer artefact subtraction (RLAS): A novel method of minimizing EEG artefacts during simultaneous fMRI. *NeuroImage*, 84, 307–319. <https://doi.org/10.1016/j.neuroimage.2013.08.039>
- Cohen, J. (1962). The statistical power of abnormal-social psychological research: A review. *Journal of Abnormal and Social Psychology*, 65, 145–153. <https://doi.org/10.1037/h0045186>
- Cohen, J. (1988). *Statistical power analysis for the behavioural sciences*. Hillsdale, NJ: Lawrence Erlbaum Associates.
- Cross, N., Paquola, C., Pomares, F. B., Perrault, A. A., Jegou, A., Nguyen, A., ... Dang-Vu, T. T. (2021). Cortical gradients of functional connectivity are robust to state-dependent changes following sleep deprivation. *NeuroImage*, 226, 117547. <https://doi.org/10.1016/j.neuroimage.2020.117547>
- Dang-Vu, T. T., Bonjean, M., Schabus, M., Boly, M., Darsaud, A., Desseilles, M., ... Maquet, P. (2011). Interplay between spontaneous and induced brain activity during human non-rapid eye movement sleep. *Proceedings of the National Academy of Sciences of the United States of America*, 108, 15438–15443. <https://doi.org/10.1073/pnas.1112503108>
- Dang-Vu, T. T., Schabus, M., Desseilles, M., Albouy, G., Boly, M., Darsaud, A., ... Maquet, P. (2008). Spontaneous neural activity during human slow wave sleep. *Proceedings of the National Academy of Sciences of the United States of America*, 105, 15160–15165. <https://doi.org/10.1073/pnas.0801819105>
- Darvas, F., Scherer, R., Ojemann, J. G., Rao, R. P., Miller, K. J., & Sorensen, L. B. (2010). High gamma mapping using EEG. *NeuroImage*, 49, 930–938. <https://doi.org/10.1016/j.neuroimage.2009.08.041>
- Debener, S., Mullinger, K. J., Niaz, R. K., & Bowtell, R. W. (2008). Properties of the ballistocardiogram artefact as revealed by EEG recordings at 1.5, 3 and 7 T static magnetic field strength. *International Journal of Psychophysiology*, 67, 189–199. <https://doi.org/10.1016/j.ijpsycho.2007.05.015>
- Debener, S., Strobel, A., Sorger, B., Peters, J., Kranczioch, C., Engel, A. K., & Goebel, R. (2007). Improved quality of auditory event-related potentials recorded simultaneously with 3-T fMRI: Removal of the ballistocardiogram artefact. *NeuroImage*, 34, 587–597. <https://doi.org/10.1016/j.neuroimage.2006.09.031>
- Debener, S., Ullsperger, M., Siegel, M., & Engel, A. K. (2006). Single-trial EEG-fMRI reveals the dynamics of cognitive function. *Trends in Cognitive Sciences*, 10, 558–563. <https://doi.org/10.1016/j.tics.2006.09.010>
- Debener, S., Ullsperger, M., Siegel, M., Fiehler, K., von Cramon, D. Y., & Engel, A. K. (2005). Trial-by-trial coupling of concurrent electroencephalogram and functional magnetic resonance imaging identifies the dynamics of performance monitoring. *The Journal of Neuroscience*, 25, 11730–11737. <https://doi.org/10.1523/JNEUROSCI.3286-05.2005>
- Delorme, A., & Makeig, S. (2004). EEGLAB: An open source toolbox for analysis of single-trial EEG dynamics including independent component analysis. *Journal of Neuroscience Methods*, 134, 9–21. <https://doi.org/10.1016/j.jneumeth.2003.10.009>
- Delorme, A., Sejnowski, T., & Makeig, S. (2007). Enhanced detection of artifacts in EEG data using higher-order statistics and independent component analysis. *NeuroImage*, 34, 1443–1449. <https://doi.org/10.1016/j.neuroimage.2006.11.004>
- Eichele, T., Calhoun, V. D., Moosmann, M., Specht, K., Jongsma, M. L. A., Quiroga, R. Q., ... Hugdahl, K. (2008). Unmixing concurrent EEG-fMRI with parallel independent component analysis. *International Journal of Psychophysiology*, 67, 222–234. <https://doi.org/10.1016/j.ijpsycho.2007.04.010>
- Eichele, T., Specht, K., Moosmann, M., Jongsma, M. L. A., Quiroga, R. Q., Nordby, H., & Hugdahl, K. (2005). Assessing the spatiotemporal evolution of neuronal activation with single-trial event-related potentials and functional MRI. *Proceedings of the National Academy of Sciences of the United States of America*, 102, 17798–17803. <https://doi.org/10.1073/pnas.0505508102>
- Fan, J., Byrne, J., Worden, M. S., Guise, K. G., McCandliss, B. D., Fossella, J., & Posner, M. I. (2007). The relation of brain oscillations to attentional networks. *The Journal of Neuroscience*, 27, 6197–6206. <https://doi.org/10.1523/JNEUROSCI.1833-07.2007>
- Fan, J., McCandliss, B., Fossella, J., Flombaum, J., & Posner, M. (2005). The activation of attentional networks. *NeuroImage*, 26, 471–479. <https://doi.org/10.1016/j.neuroimage.2005.02.004>
- Fan, J., McCandliss, B. D., Sommer, T., Raz, A., & Posner, M. I. (2002). Testing the efficiency and independence of attentional networks. *Journal of Cognitive Neuroscience*, 14, 340–347. <https://doi.org/10.1162/089892902317361886>
- Fuchs, M., Kastner, J., Wagner, M., Hawes, S., & Ebersole, J. S. (2002). A standardized boundary element method volume conductor model. *Clinical Neurophysiology*, 113, 702–712. [https://doi.org/10.1016/S1388-2457\(02\)00030-5](https://doi.org/10.1016/S1388-2457(02)00030-5)
- Fultz, N. E., Bonmassar, G., Setsompop, K., Stickgold, R. A., Rosen, B. R., Polimeni, J. R., & Lewis, L. D. (2019). Coupled electrophysiological, hemodynamic, and cerebrospinal fluid oscillations in human sleep. *Science*, 366, 628–631. <https://doi.org/10.1126/science.aax5440>
- Goldman, R. I., Stern, J. M., Engel Jerome, J., & Cohen, M. S. (2002). Simultaneous EEG and fMRI of the alpha rhythm. *Neuroreport*, 13, 2487–2492. <https://doi.org/10.1097/01.wnr.0000047685.08940.d0>
- Goldman, R. I., Wei, C. Y., Philiastides, M. G., Gerson, A. D., Friedman, D., Brown, T. R., & Sajda, P. (2009). Single-trial discrimination for integrating simultaneous EEG and fMRI: Identifying cortical areas contributing to trial-to-trial variability in the auditory oddball task. *NeuroImage*, 47, 136–147. <https://doi.org/10.1016/j.neuroimage.2009.03.062>
- Gotman, J., Kobayashi, E., Bagshaw, A. P., Bénar, C.-G., & Dubeau, F. (2006). Combining EEG and fMRI: A multimodal tool for epilepsy research. *Journal of Magnetic Resonance Imaging*, 23, 906–920. <https://doi.org/10.1002/jmri.20577>
- Gotman, J., & Pittau, F. (2011). Combining EEG and fMRI in the study of epileptic discharges. *Epilepsia*, 52, 38–42. <https://doi.org/10.1111/j.1528-1167.2011.03151.x>
- Gramfort, A., Papadopoulos, T., Olivi, E., & Clerc, M. (2010). OpenMEEG: Opensource software for quasistatic bioelectromagnetics. *Biomedical Engineering Online*, 9, 45. <https://doi.org/10.1186/1475-925X-9-45>
- Gross, J., Baillet, S., Barnes, G. R., Henson, R. N., Hillebrand, A., Jensen, O., ... Schoffelen, J.-M. (2013). Good practice for conducting and reporting MEG research. *NeuroImage*, 65, 349–363. <https://doi.org/10.1016/j.neuroimage.2012.10.001>
- Gross, J., Kujala, J., Hamalainen, M., Timmermann, L., Schnitzler, A., & Salmelin, R. (2001). Dynamic imaging of coherent sources: Studying neural interactions in the human brain. *Proceedings of the National Academy of Sciences of the United States of America*, 98, 694–699. <https://doi.org/10.1073/pnas.98.2.694>
- Grouiller, F., Thornton, R. C., Groening, K., Spinelli, L., Duncan, J. S., Schaller, K., ... Vuilleumoz, S. (2011). With or without spikes: Localization of focal epileptic activity by simultaneous electroencephalography and functional magnetic resonance imaging. *Brain*, 134, 2867–2886. <https://doi.org/10.1093/brain/awr156>

- Grova, C., Daunizeau, J., Kobayashi, E., Bagshaw, A. P., Lina, J. M., Dubeau, F., & Gotman, J. (2008). Concordance between distributed EEG source localization and simultaneous EEG-fMRI studies of epileptic spikes. *NeuroImage*, 39, 755–774. <https://doi.org/10.1016/j.neuroimage.2007.08.020>
- Hale, J. R., White, T. P., Mayhew, S. D., Wilson, R. S., Rollings, D. T., Khalsa, S., ... Bagshaw, A. P. (2016). Altered thalamocortical and intrathalamic functional connectivity during light sleep compared with wake. *NeuroImage*, 125, 657–667. <https://doi.org/10.1016/j.neuroimage.2015.10.041>
- Hall, S. D., Stanford, I. M., Yamawaki, N., McAllister, C. J., Ronnqvist, K. C., Woodhall, G. L., & Furlong, P. L. (2011). The role of GABAergic modulation in motor function related neuronal network activity. *NeuroImage*, 56, 1506–1510. <https://doi.org/10.1016/j.neuroimage.2011.02.025>
- Heers, M., Hedrich, T., An, D., Dubeau, F., Gotman, J., Grova, C., & Kobayashi, E. (2014). Spatial correlation of hemodynamic changes related to interictal epileptic discharges with electric and magnetic source imaging. *Human Brain Mapping*, 35, 4396–4414. <https://doi.org/10.1002/hbm.22482>
- Hill, R. M., Boto, E., Rea, M., Holmes, N., Leggett, J., Coles, L. A., ... Brookes, M. J. (2020). Multi-channel whole-head OPM-MEG: Helmet design and a comparison with a conventional system. *NeuroImage*, 219, 116995. <https://doi.org/10.1016/j.neuroimage.2020.116995>
- Hillebrand, A., & Barnes, G. R. (2005). Beamformer analysis of MEG data. *International Review of Neurobiology*, 68, 149–171. [https://doi.org/10.1016/S0074-7742\(05\)68006-3](https://doi.org/10.1016/S0074-7742(05)68006-3)
- Hillebrand, A., Barnes, G. R., Bosboom, J. L., Berendse, H. W., & Stam, C. J. (2012). Frequency-dependent functional connectivity within resting-state networks: An atlas-based MEG beamformer solution. *NeuroImage*, 59, 3909–3921. <https://doi.org/10.1016/j.neuroimage.2011.11.005>
- Hillebrand, A., Tewarie, P., van Dellen, E., Yu, M., Carbo, E. W. S., Douw, L., ... Stam, C. J. (2016). Direction of information flow in large-scale resting-state networks is frequency-dependent. *Proceedings of the National Academy of Sciences of the United States of America*, 113, 3867–3872. <https://doi.org/10.1073/pnas.1515657113>
- Horowitz, S. G., Fukunaga, M., de Zwart, J. A., van Gelderen, P., Fulton, S. C., Balkin, T. J., & Duyn, J. H. (2008). Low frequency BOLD fluctuations during resting wakefulness and light sleep: A simultaneous EEG-fMRI study. *Human Brain Mapping*, 29, 671–682. <https://doi.org/10.1002/hbm.20428>
- Huang, M.-X., Shih, J. J., Lee, R. R., Harrington, D. L., Thoma, R. J., Weisend, M. P., ... Canive, J. M. (2004). Commonalities and differences among vectorized beamformers in electromagnetic source imaging. *Brain Topography*, 16, 139–158. <https://doi.org/10.1023/B:BRAT.0000019183.92439.51>
- Huster, R. J., Debener, S., Eichele, T., & Herrmann, C. S. (2012). Methods for simultaneous EEG-fMRI: An introductory review. *The Journal of Neuroscience*, 32, 6053–6060. <https://doi.org/10.1523/JNEUROSCI.0447-12.2012>
- Iannotti, G. R., Pittau, F., Michel, C. M., Vuillemoz, S., & Grouiller, F. (2015). Pulse artifact detection in simultaneous EEG-fMRI recording based on EEG map topography. *Brain Topography*, 28, 21–32. <https://doi.org/10.1007/s10548-014-0409-z>
- Ives, J. R., Warach, S., Schmitt, F., Edelman, R. R., & Schomer, D. L. (1993). Monitoring the patient's EEG during echo planar MRI. *Electroencephalography and Clinical Neurophysiology*, 87, 417–420. [https://doi.org/10.1016/0013-4694\(93\)90156-P](https://doi.org/10.1016/0013-4694(93)90156-P)
- Jorge, J., Boulou, C., Bréchet, L., Michel, C. M., & Gruetter, R. (2019). Investigating the variability of cardiac pulse artifacts across heartbeats in simultaneous EEG-fMRI recordings: A 7T study. *NeuroImage*, 191, 21–35. <https://doi.org/10.1016/j.neuroimage.2019.02.021>
- Jorge, J., van der Zwaag, W., & Figueiredo, P. (2014). EEG-fMRI integration for the study of human brain function. *NeuroImage*, 102, 24–34. <https://doi.org/10.1016/j.neuroimage.2013.05.114>
- Kirchner, W. K. (1958). Age differences in short-term retention of rapidly changing information. *Journal of Experimental Psychology*, 55, 352–358. <https://doi.org/10.1037/h0043688>
- Kybic, J., Clerc, M., Faugeras, O., Keriven, R., & Papadopoulos, T. (2006). Generalized head models for MEG/EEG: Boundary element method beyond nested volumes. *Physics in Medicine and Biology*, 51, 1333–1346. <https://doi.org/10.1088/0031-9155/51/5/021>
- Laufs, H. (2012). A personalized history of EEG-fMRI integration. *NeuroImage*, 62, 1056–1067. <https://doi.org/10.1016/j.neuroimage.2012.01.039>
- Laufs, H., Daunizeau, J., Carmichael, D. W., & Kleinschmidt, A. (2008). Recent advances in recording electrophysiological data simultaneously with magnetic resonance imaging. *NeuroImage*, 40, 515–528. <https://doi.org/10.1016/j.neuroimage.2007.11.039>
- Laufs, H., Kleinschmidt, A., Beyerle, A., Eger, E., Salek-Haddadi, A., Preibisch, C., & Krakow, K. (2003). EEG-correlated fMRI of human alpha activity. *NeuroImage*, 19, 1463–1476. [https://doi.org/10.1016/S1053-8119\(03\)00286-6](https://doi.org/10.1016/S1053-8119(03)00286-6)
- Lemieux, L., Salek-Haddadi, A., Josephs, O., Allen, P., Toms, N., Scott, C., ... Fish, D. R. (2001). Event-related fMRI with simultaneous and continuous EEG: Description of the method and initial case report. *NeuroImage*, 14, 780–787. <https://doi.org/10.1006/nimg.2001.0853>
- LeVan, P., & Gotman, J. (2009). Independent component analysis as a model-free approach for the detection of BOLD changes related to epileptic spikes: A simulation study. *Human Brain Mapping*, 30, 2021–2031. <https://doi.org/10.1002/hbm.20647>
- LeVan, P., Maclaren, J., Herbst, M., Sostheim, R., Zaitsev, M., & Hennig, J. (2013). Ballistocardiographic artifact removal from simultaneous EEG-fMRI using an optical motion-tracking system. *NeuroImage*, 75, 1–11. <https://doi.org/10.1016/j.neuroimage.2013.02.039>
- Lichstein, K. L., Riedel, B. W., & Richman, S. L. (2000). The Mackworth clock test: A computerized version. *The Journal of Psychology*, 134, 153–161. <https://doi.org/10.1080/00223980009600858>
- Litvak, V., Eusebio, A., Jha, A., Oostenveld, R., Barnes, G. R., Penny, W. D., ... Brown, P. (2010). Optimized beamforming for simultaneous MEG and intracranial local field potential recordings in deep brain stimulation patients. *NeuroImage*, 50, 1578–1588. <https://doi.org/10.1016/j.neuroimage.2009.12.115>
- Logothetis, N. K., Pauls, J., Augath, M., Trinath, T., & Oeltermann, A. (2001). Neurophysiological investigation of the basis of the fMRI signal. *Nature*, 412, 150–157. <https://doi.org/10.1038/35084005>
- Loh, S., Lamond, N., Dorrian, J., Roach, G., & Dawson, D. (2004). The validity of psychomotor vigilance tasks of less than 10-minute duration. *Behavior Research Methods, Instruments, & Computers*, 36, 339–346. <https://doi.org/10.3758/BF03195580>
- Mantini, D., Perrucci, M. G., Cugini, S., Ferretti, A., Romani, G. L., & del Gratta, C. (2007). Complete artifact removal for EEG recorded during continuous fMRI using independent component analysis. *NeuroImage*, 34, 598–607. <https://doi.org/10.1016/j.neuroimage.2006.09.037>
- Marino, M., Liu, Q., Koudelka, V., Porcaro, C., Hlinka, J., Wenderoth, N., & Mantini, D. (2018). Adaptive optimal basis set for BCG artifact removal in simultaneous EEG-fMRI. *Scientific Reports*, 8, 8902. <https://doi.org/10.1038/s41598-018-27187-6>
- Maris, E. (2012). Statistical testing in electrophysiological studies. *Psychophysiology*, 49, 549–565. <https://doi.org/10.1111/j.1469-8986.2011.01320.x>
- Maris, E., & Oostenveld, R. (2007). Nonparametric statistical testing of EEG- and MEG-data. *Journal of Neuroscience Methods*, 164, 177–190. <https://doi.org/10.1016/j.jneumeth.2007.03.024>
- Marshall, T. R., Bergmann, T. O., & Jensen, O. (2015). Frontoparietal structural connectivity mediates the top-down control of neuronal synchronization associated with selective attention. *PLoS Biology*, 13, e1002272. <https://doi.org/10.1371/journal.pbio.1002272>

- Masterton, R. A. J., Abbott, D. F., Fleming, S. W., & Jackson, G. D. (2007). Measurement and reduction of motion and ballistocardiogram artefacts from simultaneous EEG and fMRI recordings. *NeuroImage*, 37, 202–211. <https://doi.org/10.1016/j.neuroimage.2007.02.060>
- Mayhew, S. D., Li, S., & Kourtzi, Z. (2012). Learning acts on distinct processes for visual form perception in the human brain. *The Journal of Neuroscience*, 32, 775–786. <https://doi.org/10.1523/JNEUROSCI.2033-11.2012>
- Mayhew, S. D., Ostwald, D., Porcaro, C., & Bagshaw, A. P. (2013). Spontaneous EEG alpha oscillation interacts with positive and negative BOLD responses in the visual-auditory cortices and default-mode network. *NeuroImage*, 76, 362–372. <https://doi.org/10.1016/j.neuroimage.2013.02.070>
- Mobascher, A., Brinkmeyer, J., Warbrick, T., Musso, F., Wittsack, H. J., Saleh, A., ... Winterer, G. (2009). Laser-evoked potential P2 single-trial amplitudes covary with the fMRI BOLD response in the medial pain system and interconnected subcortical structures. *NeuroImage*, 45, 917–926. <https://doi.org/10.1016/j.neuroimage.2008.12.051>
- Moeller, F., Siniatchkin, M., & Gotman, J. (2020). Simultaneous EEG and fMRI recordings (EEG–fMRI). In *fMRI* (pp. 175–191). Cham: Springer International Publishing. https://doi.org/10.1007/978-3-030-41874-8_13
- Mullinger, K. J., & Bowtell, R. (2011). Combining EEG and fMRI. *Methods in Molecular Biology*, 711, 303–326. https://doi.org/10.1007/978-1-61737-992-5_15
- Mullinger, K. J., Brookes, M., Stevenson, C., Morgan, P., & Bowtell, R. (2008). Exploring the feasibility of simultaneous electroencephalography/functional magnetic resonance imaging at 7 T. *Magnetic Resonance Imaging*, 26, 968–977. <https://doi.org/10.1016/j.mri.2008.02.014>
- Mullinger, K. J., Cherukara, M. T., Buxton, R. B., Francis, S. T., & Mayhew, S. D. (2017). Post-stimulus fMRI and EEG responses: Evidence for a neuronal origin hypothesised to be inhibitory. *NeuroImage*, 157, 388–399. <https://doi.org/10.1016/j.neuroimage.2017.06.020>
- Mullinger, K. J., Mayhew, S. D., Bagshaw, A. P., Bowtell, R., & Francis, S. T. (2013). Poststimulus undershoots in cerebral blood flow and BOLD fMRI responses are modulated by poststimulus neuronal activity. *Proceedings of the National Academy of Sciences of the United States of America*, 110, 13636–13641. <https://doi.org/10.1073/pnas.1221287110>
- Mullinger, K. J., Mayhew, S. D., Bagshaw, A. P., Bowtell, R., & Francis, S. T. (2014). Evidence that the negative BOLD response is neuronal in origin: A simultaneous EEG–BOLD–CBF study in humans. *NeuroImage*, 94, 263–274. <https://doi.org/10.1016/j.neuroimage.2014.02.029>
- Mullinger, K. J., Morgan, P. S., & Bowtell, R. W. (2008). Improved artifact correction for combined electroencephalography/functional MRI by means of synchronization and use of vectorcardiogram recordings. *Journal of Magnetic Resonance Imaging*, 27, 607–616. <https://doi.org/10.1002/jmri.21277>
- Murta, T., Leal, A., Garrido, M. I., & Figueiredo, P. (2012). Dynamic causal modelling of epileptic seizure propagation pathways: A combined EEG–fMRI study. *NeuroImage*, 62, 1634–1642. <https://doi.org/10.1016/j.neuroimage.2012.05.053>
- Murta, T., Leite, M., Carmichael, D. W., Figueiredo, P., & Lemieux, L. (2015). Electrophysiological correlates of the BOLD signal for EEG-informed fMRI. *Human Brain Mapping*, 36, 391–414. <https://doi.org/10.1002/hbm.22623>
- Muthukumaraswamy, S. D. (2010). Functional properties of human primary motor cortex gamma oscillations. *Journal of Neurophysiology*, 104, 2873–2885. <https://doi.org/10.1152/jn.00607.2010>
- Neugebauer, F., Möddel, G., Rampp, S., Burger, M., & Wolters, C. H. (2017). The effect of head model simplification on beamformer source localization. *Frontiers in Neuroscience*, 11, 1–15. <https://doi.org/10.3389/fnins.2017.00625>
- Niazy, R. K., Beckmann, C. F., Iannetti, G. D., Brady, J. M., & Smith, S. M. (2005). Removal of fMRI environment artifacts from EEG data using optimal basis sets. *NeuroImage*, 28, 720–737. <https://doi.org/10.1016/j.neuroimage.2005.06.067>
- Nichols, T. E., & Holmes, A. P. (2002). Nonparametric permutation tests for functional neuroimaging: A primer with examples. *Human Brain Mapping*, 15, 1–25. <https://doi.org/10.1002/hbm.1058>
- Novitskiy, N., Ramautar, J. R., Vanderperren, K., de Vos, M., Mennes, M., Mijovic, B., ... Wagemans, J. (2011). The BOLD correlates of the visual P1 and N1 in single-trial analysis of simultaneous EEG–fMRI recordings during a spatial detection task. *NeuroImage*, 54, 824–835. <https://doi.org/10.1016/j.neuroimage.2010.09.041>
- Olbrich, S., Mulert, C., Karch, S., Trenner, M., Leicht, G., Pogarell, O., & Hegerl, U. (2009). EEG–vigilance and BOLD effect during simultaneous EEG/fMRI measurement. *NeuroImage*, 45, 319–332. <https://doi.org/10.1016/j.neuroimage.2008.11.014>
- Oostendorp, T., & van Oosterom, A. (1991). The potential distribution generated by surface electrodes in inhomogeneous volume conductors of arbitrary shape. *IEEE Transactions on Biomedical Engineering*, 38, 409–417. <https://doi.org/10.1109/10.81559>
- Oostenveld, R., Fries, P., Maris, E., & Schoffelen, J. M. (2011). FieldTrip: Open source software for advanced analysis of MEG, EEG, and invasive electrophysiological data. *Computational Intelligence and Neuroscience*, 2011, 156869. <https://doi.org/10.1155/2011/156869>
- Pakenham, D. O., Quinn, A. J., Fry, A., Francis, S. T., Woolrich, M. W., Brookes, M. J., & Mullinger, K. J. (2020). Post-stimulus beta responses are modulated by task duration. *NeuroImage*, 206, 116288. <https://doi.org/10.1016/j.neuroimage.2019.116288>
- Pfurtscheller, G., & Lopes da Silva, F. H. (1999). Event-related EEG/MEG synchronization and desynchronization: Basic principles. *Clinical Neurophysiology*, 110, 1842–1857. [https://doi.org/10.1016/S1388-2457\(99\)00141-8](https://doi.org/10.1016/S1388-2457(99)00141-8)
- Pfurtscheller, G., Stancák, A., & Neuper, C. (1996). Post-movement beta synchronization. A correlate of an idling motor area? *Electroencephalography and Clinical Neurophysiology*, 98, 281–293. [https://doi.org/10.1016/0013-4694\(95\)00258-8](https://doi.org/10.1016/0013-4694(95)00258-8)
- Quraan, M. A., & Cheyne, D. (2010). Reconstruction of correlated brain activity with adaptive spatial filters in MEG. *NeuroImage*, 49, 2387–2400. <https://doi.org/10.1016/j.neuroimage.2009.10.012>
- Robinson, S. E., & Vrba, J. (1999). Functional neuroimaging by synthetic aperture magnetometry (SAM). In T. Yoshimoto, M. Kotani, S. Kuriki, H. Karibe, & N. Nakasato (Eds.), *Recent advances in biomagnetism* (pp. 302–305). Sendai, Japan: Tohoku University Press.
- Rothlübbers, S., Relvas, V., Leal, A., Murta, T., Lemieux, L., & Figueiredo, P. (2015). Characterisation and reduction of the EEG artefact caused by the helium cooling pump in the MR environment: Validation in epilepsy patient data. *Brain Topography*, 28, 208–220. <https://doi.org/10.1007/s10548-014-0408-0>
- Russell, G. S., Jeffrey Eriksen, K., Poolman, P., Luu, P., & Tucker, D. M. (2005). Geodesic photogrammetry for localizing sensor positions in dense-array EEG. *Clinical Neurophysiology*, 116, 1130–1140. <https://doi.org/10.1016/j.clinph.2004.12.022>
- Sawilowsky, S. S. (2009). New effect size rules of thumb. *Journal of Modern Applied Statistical Methods*, 8, 597–599. <https://doi.org/10.22237/jmasm/1257035100>
- Scheeringa, R., Fries, P., Petersson, K.-M., Oostenveld, R., Grothe, I., Norris, D. G., ... Bastiaansen, M. C. M. (2011). Neuronal dynamics underlying high- and low-frequency EEG oscillations contribute independently to the human BOLD signal. *Neuron*, 69, 572–583. <https://doi.org/10.1016/j.neuron.2010.11.044>
- Scheibe, C., Ullsperger, M., Sommer, W., & Heekeren, H. R. (2010). Effects of parametrical and trial-to-trial variation in prior probability processing revealed by simultaneous electroencephalogram/functional magnetic resonance imaging. *The Journal of Neuroscience*, 30, 16709–16717. <https://doi.org/10.1523/JNEUROSCI.3949-09.2010>
- Sekihara, K., & Nagarajan, S. S. (2008). *Adaptive spatial filters for electromagnetic brain imaging, series in biomedical engineering*. Berlin: Springer Berlin Heidelberg. <https://doi.org/10.1007/978-3-540-79370-0>

- Sekihara, K., Nagarajan, S. S., Poeppel, D., & Marantz, A. (2004). Asymptotic SNR of scalar and vector minimum-variance beamformers for neuromagnetic source reconstruction. *IEEE Transactions on Biomedical Engineering*, 51, 1726–1734. <https://doi.org/10.1109/TBME.2004.827926>
- Sekihara, K., Nagarajan, S. S., Poeppel, D., Marantz, A., & Miyashita, Y. (2001). Reconstructing spatio-temporal activities of neural sources using an MEG vector beamformer technique. *IEEE Transactions on Biomedical Engineering*, 48, 760–771. <https://doi.org/10.1109/10.930901>
- Srivastava, G., Crottaz-Herbette, S., Lau, K. M., Glover, G. H., & Menon, V. (2005). ICA-based procedures for removing ballistocardiogram artifacts from EEG data acquired in the MRI scanner. *NeuroImage*, 24, 50–60. <https://doi.org/10.1016/j.neuroimage.2004.09.041>
- Sweet, L. H. (2011). N-back paradigm. In *Encyclopedia of clinical neuropsychology* (pp. 1718–1719). New York, NY: Springer New York. https://doi.org/10.1007/978-0-387-79948-3_1315
- Takemi, M., Masakado, Y., Liu, M., & Ushiba, J. (2013). Event-related desynchronization reflects downregulation of intracortical inhibition in human primary motor cortex. *Journal of Neurophysiology*, 110, 1158–1166. <https://doi.org/10.1152/jn.01092.2012>
- Tyvaert, L., LeVan, P., Grova, C., Dubeau, F., & Gotman, J. (2008). Effects of fluctuating physiological rhythms during prolonged EEG-fMRI studies. *Clinical Neurophysiology*, 119, 2762–2774. <https://doi.org/10.1016/j.clinph.2008.07.284>
- Uji, M., Jentzsch, I., Redburn, J., & Vishwanath, D. (2019). Dissociating neural activity associated with the subjective phenomenology of monocular stereopsis: An EEG study. *Neuropsychologia*, 129, 357–371. <https://doi.org/10.1016/j.neuropsychologia.2019.04.017>
- Uji, M., Wilson, R., Francis, S. T., Mullinger, K. J., & Mayhew, S. D. (2018). Exploring the advantages of multiband fMRI with simultaneous EEG to investigate coupling between gamma frequency neural activity and the BOLD response in humans. *Human Brain Mapping*, 39, 1673–1687. <https://doi.org/10.1002/hbm.23943>
- van Drongelen, W., Yuchtman, M., Van Veen, B. D., & van Huffelen, A. C. (1996). A spatial filtering technique to detect and localize multiple sources in the brain. *Brain Topography*, 9, 39–49. <https://doi.org/10.1007/BF01191641>
- van Klink, N., Mol, A., Ferrier, C., Hillebrand, A., Huiskamp, G., & Zijlmans, M. (2018). Beamforming applied to surface EEG improves ripple visibility. *Clinical Neurophysiology*, 129, 101–111. <https://doi.org/10.1016/j.clinph.2017.10.026>
- van Veen, B. D., & Buckley, K. M. (1988). Beamforming: A versatile approach to spatial filtering. *IEEE ASSP Magazine*, 5, 4–24. <https://doi.org/10.1109/53.665>
- van Veen, B. D., van Drongelen, W., Yuchtman, M., & Suzuki, A. (1997). Localization of brain electrical activity via linearly constrained minimum variance spatial filtering. *Biomédica*, 44, 867–880. <https://doi.org/10.1109/10.623056>
- Vanderperren, K., de Vos, M., Ramautar, J. R., Novitskiy, N., Mennes, M., Assecondi, S., ... van Huffel, S. (2010). Removal of BCG artifacts from EEG recordings inside the MR scanner: A comparison of methodological and validation-related aspects. *NeuroImage*, 50, 920–934. <https://doi.org/10.1016/j.neuroimage.2010.01.010>
- Vanderperren, K., Ramautar, J., Novitskiy, N., de Vos, M., Mennes, M., Vanrumste, B., ... van Huffel, S. (2007). Ballistocardiogram artifacts in simultaneous EEG-fMRI acquisitions. *International Journal of Bioelectromagnetism*, 9, 146–150.
- Wilson, R., Mullinger, K. J., Francis, S. T., & Mayhew, S. D. (2019). The relationship between negative BOLD responses and ERS and ERD of alpha/beta oscillations in visual and motor cortex. *NeuroImage*, 199, 635–650. <https://doi.org/10.1016/j.neuroimage.2019.06.009>
- Xia, H., Ruan, D., & Cohen, M. S. (2013). *Coupled basis learning and regularized reconstruction for BCG artifact removal in simultaneous EEG-fMRI studies*. Proceedings - International Symposium on Biomedical Imaging. <https://doi.org/10.1109/ISBI.2013.6556642>
- Xia, H., Ruan, D., & Cohen, M. S. (2014). Removing ballistocardiogram (BCG) artifact from full-scalp EEG acquired inside the MR scanner with orthogonal matching pursuit (OMP). *Frontiers in Neuroscience*, 8, 1–12. <https://doi.org/10.3389/fnins.2014.00218>
- Youssofzadeh, V., Agler, W., Tenney, J. R., & Kadis, D. S. (2018). Whole-brain MEG connectivity-based analyses reveals critical hubs in childhood absence epilepsy. *Epilepsy Research*, 145, 102–109. <https://doi.org/10.1016/j.eplepsyres.2018.06.001>
- Youssofzadeh, V., Williamson, B. J., & Kadis, D. S. (2017). Mapping critical language sites in children performing verb generation: Whole-brain connectivity and graph theoretical analysis in MEG. *Frontiers in Human Neuroscience*, 11, 173. <https://doi.org/10.3389/fnhum.2017.00173>

SUPPORTING INFORMATION

Additional supporting information may be found online in the Supporting Information section at the end of this article.

How to cite this article: Uji, M., Cross, N., Pomares, F. B., Perrault, A. A., Jegou, A., Nguyen, A., Aydin, U., Lina, J.-M., Dang-Vu, T. T., & Grova, C. (2021). Data-driven beamforming technique to attenuate ballistocardiogram artefacts in electroencephalography–functional magnetic resonance imaging without detecting cardiac pulses in electrocardiography recordings. *Human Brain Mapping*, 42(12), 3993–4021. <https://doi.org/10.1002/hbm.25535>